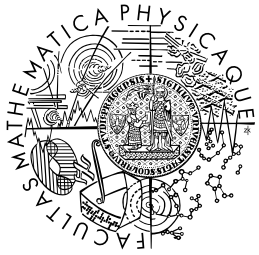


FACULTY
OF MATHEMATICS
AND PHYSICS
Charles University

**MASTER THESIS**

Tadeáš Wilczek

# Studies of the Belle II vertex detector physics performance

Institute of Particle and Nuclear Physics

Supervisor of the master thesis: prof. RNDr. Zdeněk Doležal, Dr.
Study programme: Physics
Study branch: Particle and Nuclear Physics

Prague 2025

I declare that I carried out this master thesis independently, and only with the cited sources, literature and other professional sources. It has not been used to obtain another or the same degree.

I understand that my work relates to the rights and obligations under the Act No. 121/2000 Sb., the Copyright Act, as amended, in particular the fact that the Charles University has the right to conclude a license agreement on the use of this work as a school work pursuant to Section 60 subsection 1 of the Copyright Act.

In ..... date .....  .....

Author's signature

I would like to thank my supervisor, prof. RNDr. Zdeněk Doležal, Dr., for enabling me to continue my work on the Belle II detector, for providing numerous opportunities to further interact with the Belle II collaboration, and for his patience with me during my studies.

I would also like to express my profound gratitude to my consultant RNDr. Tadeáš Bilka, Ph.D. for his countless invaluable advice, discussions about Belle II and for his consistent support and assistance with my work.

I would like to thank the entire Prague Belle II group for their support and all members of the Belle II collaboration for making this possible.

And last but not least, I would like to thank my family for still supporting me and always being there for me.

Title: Studies of the Belle II vertex detector physics performance

Author: Tadeáš Wilczek

Department: Institute of Particle and Nuclear Physics

Supervisor: prof. RNDr. Zdeněk Doležal, Dr., Institute of Particle and Nuclear Physics

Abstract: The goal of this thesis is to study the performance of the Belle II vertex detector. The first part gives a brief physics motivation and introduces the Belle II experiment, then the entire detector is described. The following chapter explains the parametrization used. Then the performance of the detector is examined using muons from cosmic radiation while its magnetic field was turned off shortly after PXD commissioning. The next chapter uses muons from collisions to study the detector. It starts with a Monte Carlo simulation and then follows by comparing it to recent data measured during the year 2024. And at the end the resolution of the detector while PXD was turned off was determined. The outcome of the thesis is the resolution of the detector and a python script that can be used to verify the performance of the detector in the future.

Keywords: Belle II, vertex detector, alignment, resolution.

# Contents

# Introduction

Particle physics is a science focused on understanding the elementary building blocks of the universe (elementary particles). The main goal is to find and fully describe all of them and their interactions. With such knowledge, we could theoretically construct a comprehensive understanding of the universe.

## The Standard Model

The Standard Model (SM) is the current leading theory containing most of our knowledge of the subatomic world. It describes three fundamental forces (strong, weak and electromagnetic interactions) and all known elementary particles. The particles are categorized into groups based on their properties: fermions (quarks and leptons) and bosons (vector and scalar). This is illustrated in Fig. 1.

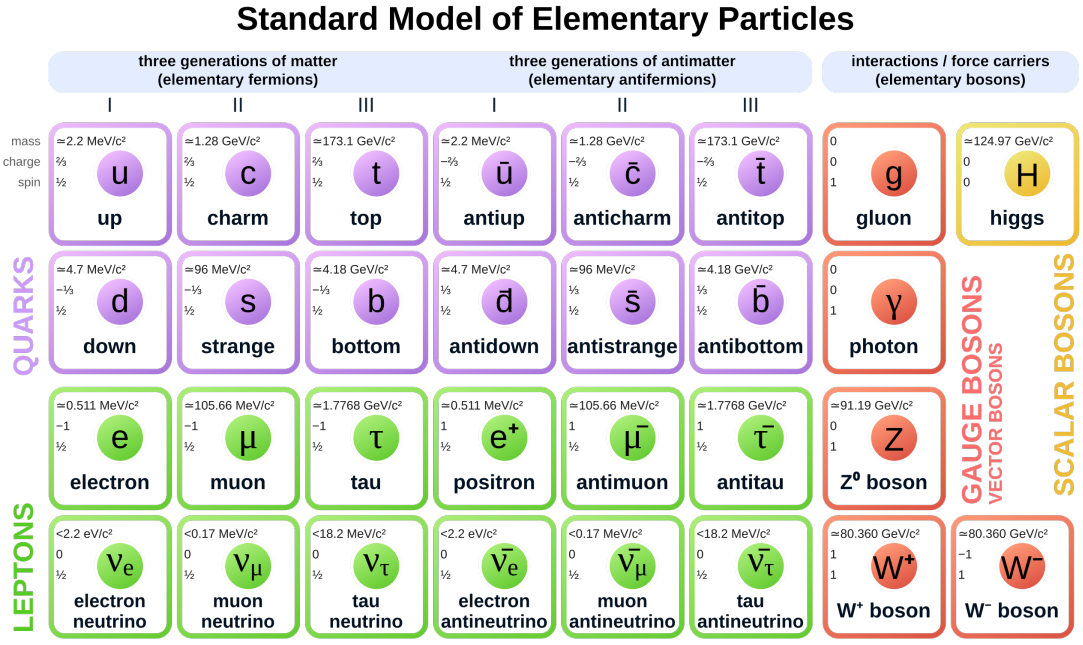


Figure 1: Elementary particles of the Standard Model [1]

However, despite its immense success, the Standard Model is incomplete. There are several phenomena that have been observed but cannot be explained by the Standard Model in its current form.

For example the fundamental force of gravity is completely missing. Another mystery is the abundance of matter compared to antimatter in the world. This could potentially be explained by the so-called CP violation.

### The CP Violation

It is the violation of the combined symmetries of charge conjugation (C-symmetry) and parity (P-symmetry).

The C-symmetry states that the physical laws shouldn't change if we perform a charge conjugation. This for example can be understood as exchanging the particle for its antiparticle.

The P-symmetry refers to the fact that particle physics equations should be invariant under mirror inversion. This can be tested by comparing the rate at which the mirror image of a reaction occurs to that of the original reaction.

Both of these symmetries have been previously thought to hold on their own. However, it was discovered that the weak interaction violates both of them. Later, using kaon decays, it was shown that the weak interaction violates even the combined CP-symmetry [2, 3]. In the Standard Model CP violation can be explained by introducing a complex phase into the Cabibbo-Kobayashi-Maskawa (CKM) matrix [4].

However, the effect of the complex phase in the CKM matrix is several orders of magnitude too weak to properly explain the large dominance of matter we have observed [5]. This discrepancy led to an extensive effort to study the CP violation in greater detail in order to uncover its secrets.

The desire to observe the CP violation in different systems (decays of B mesons) led to the rise of a whole new generation of experiments called "B-factories". Namely, the BaBar experiment and the Belle experiment. Belle II is a successor to the original Belle experiment and is currently the only "next-generation" B-factory in operation. (There is also the LHCb experiment at CERN that focuses on bottom-quark containing hadrons, but it is typically not referred to as a B-factory.)

This thesis will focus on analyzing the Belle II detector performance, specifically on its vertex detector, as it is essential for determining the momenta and positions of the particles. In chapter 1 we will describe the Belle II experiment and the detector. Then in the chapter 2 we will explain our methods and in the following chapters 3 and 4 we will apply those methods to data and simulations of cosmic radiation and muons from collisions respectively.

# 1. The Belle II experiment

The Belle II experiment is located at the SuperKEKB particle accelerator (shown in Fig. 1.1) at KEK in Tsukuba, Ibaraki Prefecture, Japan. It collides 7 GeV electrons $e^-$ with 4 GeV positrons $e^+$. The total center-of-mass (CMS) energy corresponds to the $\Upsilon(4S)$ resonance. The purpose of the asymmetric energies is to provide a boost to the CMS system and allow for time-dependent CP violation measurements [5].

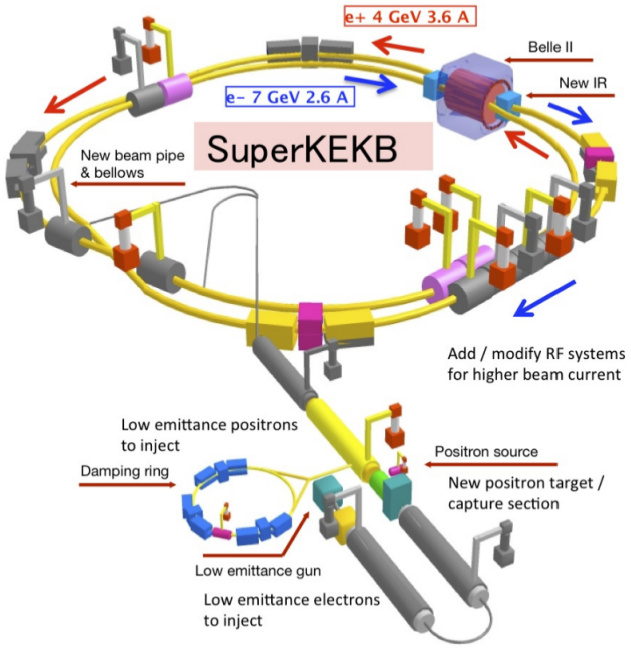


Figure 1.1: Schematic view of the SuperKEKB collider [6].

The main goals of Belle II are to search for New Physics (NP) in the flavor sector at the intensity frontier, and to improve the precision of measurements of the SM parameters. The mass reach for new particle/process effects of Belle II can under certain conditions be as high as $\mathcal{O}(100\,\text{TeV})$. For comparison, at the energy frontier, the LHC experiments can discover new particles at CMS energy of up to 14 TeV [5].

The target luminosity of SuperKEKB is designed to be 40 times greater than the recorded peak of KEKB. This is achieved by reducing the beam size at the collision point 20 times and increasing the currents by a factor of 2. The reduced beam size at the collision point at Belle II is called the "nano-beam" scheme and the shape of the beams is illustrated in Fig. 1.2.

## 1.1 The Belle II detector

The Belle II detector (shown in Fig. 1.3 together with a silhouette of a person for scale) is a complex piece of equipment that consists of many parts. In the following text we will briefly describe the most important of them. We will focus on the Vertex Detector in the greatest detail (chapter 1.2) and the remaining

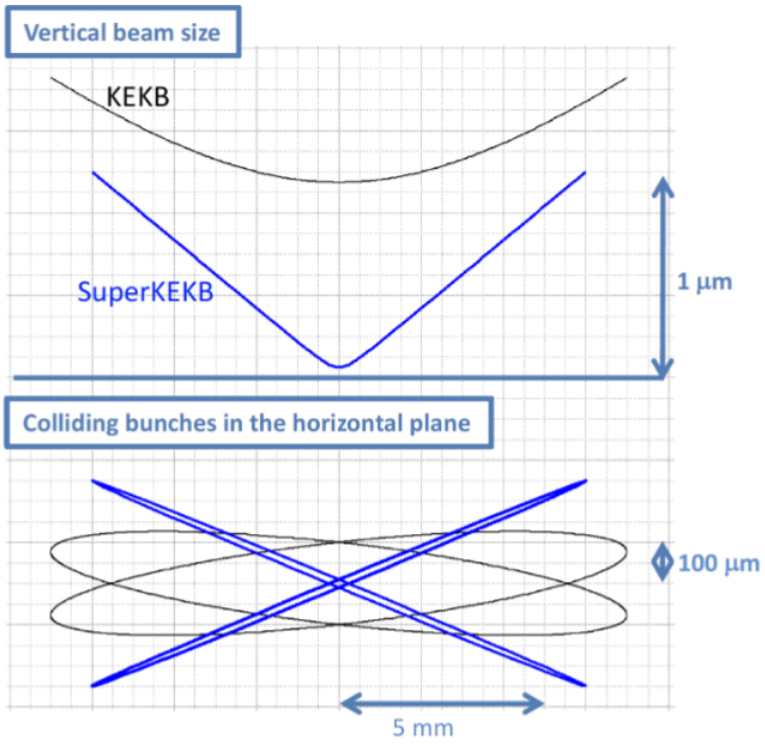


Figure 1.2: Comparison of the beam scheme at SuperKEKB (blue) with the older scheme from KEKB (black). [7]

parts (chapters 1.3 - 1.6) will be described only briefly as they are not the main focus of this thesis.

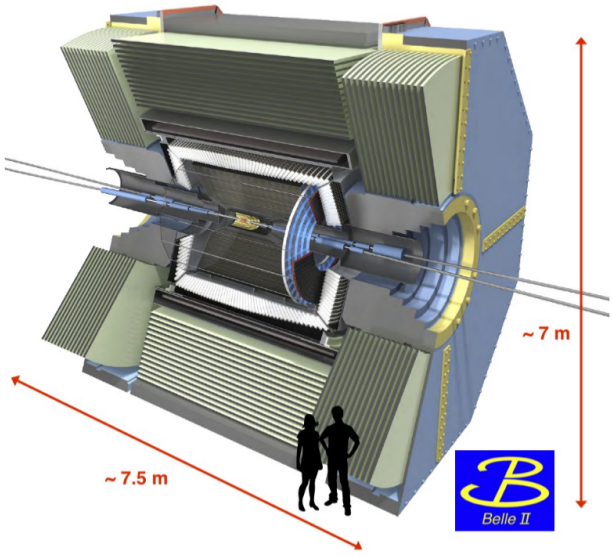


Figure 1.3: Schematic view of the Belle II detector. [6]

## 1.2 The Vertex Detector (VXD)

The Vertex Detector was one of the parts of the Belle that received the most substantial changes during the upgrade to Belle II. SuperKEKB has a design luminosity of $8 \times 10^{35}/(\mathrm{cm}^2\,\mathrm{s})$ and due to this increase compared to KEKB strip detectors can only be used beyond a 40 mm radius. The large occupancy would make vertex reconstruction impossible [8]. This issue can be addressed by employing pixel detectors at the smaller radii instead. They have much larger number of channels and therefore lower occupancy. The vertex resolution of the VXD should be at least 50 µm [5].

The VXD consists of two inner layers of silicon pixel detectors at radii 14 mm and 22 mm and four layers of double-sided silicon strip detectors at 38 mm, 80 mm, 115 mm and 140 mm.

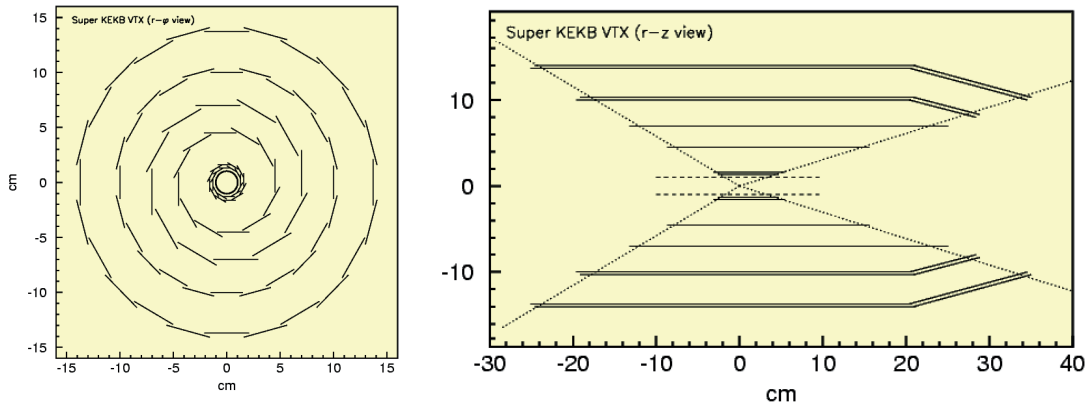


Figure 1.4: Schematic view of the Belle II vertex detector. [8]

The front modules in the two outermost layers of the SVD are angled to improve the resolution and get a better angular coverage as can be seen in Fig. 1.4. This is necessary because due to the boost of the CMS system a significant portion of outgoing particles travel in the forward direction.

### 1.2.1 Pixel Detector (PXD)

The PXD consists of two layers of silicon pixel detectors at radii 14 mm and 22 mm and the support structure holding them is mounted directly to the beampipe. Due to the low energies at SuperKEKB (compared to LHC) the pixel detectors used at other experiments are too thick. The multiple scattering effects would make precise reconstruction of B-decay vertices impossible [8]. So at Belle II the Depleted Field Effect Transistor (DEPFET) technology was used instead. It combines detection and amplification within one device. The operation principle is shown in Fig. 1.5, it allows for detectors as thin as 50 µm. With this technology the readout electronics together with active cooling can be located outside the acceptance region and do not contribute to the multiple scattering. For the detectors themselves air cooling is sufficient [8].

The inner layer consists of 8 planar sensors, each 15 mm wide with a 90 mm long sensitive area composed of 50 µm × 50 µm pixels. The outer layer consists of 12 modules also 15 mm wide with a 123 mm long sensitive area composed of

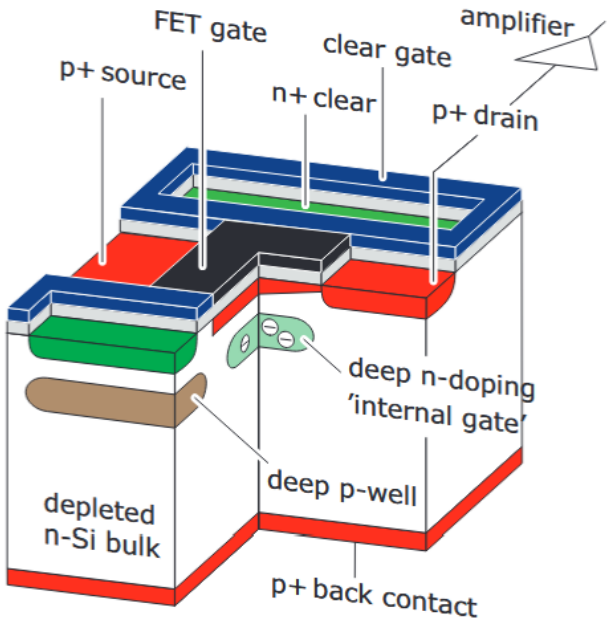


Figure 1.5: Operating principle of a DEPFET pixel. [8]

50 µm × 75 µm pixels. The total polar angle range covered is 17° to 150° as seen in the right part of Fig. 1.4. The readout is done in rows with four rows processed in parallel.

### 1.2.2 Silicon Vertex Detector (SVD)

The main purpose of the SVD, PXD and CDC at Belle II is to measure the decay vertices of the two B mesons for the measurement of mixing-induced CP asymmetry. The SVD also measures vertex information in D-meson and $\tau$-lepton decays [5].

The SVD consists of four layers of double-sided silicon strip detectors at radii of 38 mm, 80 mm, 115 mm and 140 mm. It has 8, 10, 14 and 17 ladders in each layer correspondingly. There is about 8 % to 10 % (depending on the layer) overlap of the sensor area between ladders. This may explain the regular "stripes" we can see in Fig. 4.8. More discussion on this topic will be done in chapter 4.

## 1.3 Central Drift Chamber (CDC)

The Central Drift Chamber is a large volume drift chamber with small drift cells. It starts after the VXD and extends to a radius of 1130 mm. To handle the higher luminosities the drift cells are smaller compared to Belle. It has 14 336 sense wires in 56 layers [5]. It fulfills three important roles: reconstruction of charged tracks and measurement of their momenta, particle identification using the energy loss within its gas volume and is the source of trigger signals for charged particles [8].

## 1.4 Particle Identification (PID)

The particle identification system at Belle II consists of two different sub-detectors. A Time of Propagation Counter (TOP) in the barrel region and an Aerogel Ring-Imaging Cherenkov Detector (ARICH) in the forward end-cap region. Both systems use Cherenkov radiation, emitted by charged particles traveling faster than the speed of light in a given medium, for particle identification. The main purpose of the PID is to separate kaons and pions over most of their momentum spectrum and to distinguish pions, muons, and electrons below 1 GeV/$c$ [8].

### 1.4.1 Time of Propagation Counter (TOP)

Time of Propagation Counter is a special kind of Cherenkov detector where the 2D information of a Cherenkov ring image is captured by measuring a time of arrival and impact position of Cherenkov photons at a photo-detector at one end of a quartz bar. Each module consists of a 2.6 m long, 45 cm wide and 2 cm thick quartz bar with a small expansion volume at the detector end of the bar [5].

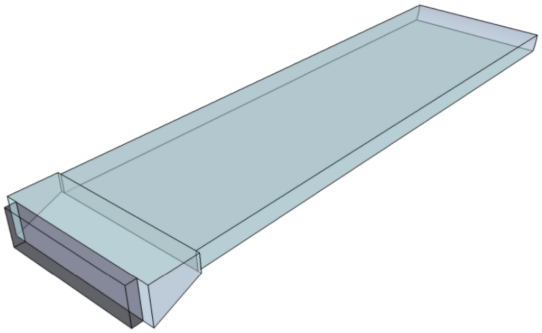

Figure 1.6: Schematic representation of one of the TOP modules. [5]

### 1.4.2 Aerogel Ring-Imaging Cherenkov Detector (ARICH)

ARICH is a proximity focusing Cherenkov ring imaging detector with aerogel as Cherenkov radiator. It's located in the forward end-cap region of the Belle II detector. The principle behind its function is illustrated in Fig. 1.7. Two 2 cm thick layers of aerogel with different refractive indices are used to increase the number of Cherenkov photons produced without degrading the Cherenkov angle resolution [5].

## 1.5 Electromagnetic Calorimeter (ECL)

The main function of the ECL is to detect gamma rays and to distinguish electrons from hadrons. It consists of highly-segmented CsI(Tl) crystals in three regions, the barrel and the forward and backward end-caps. In total, it covers 90 % of the solid angle in the CMS system [5].

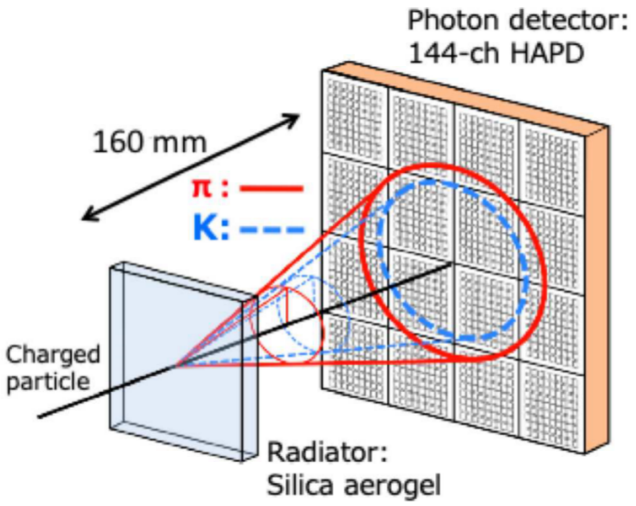


Figure 1.7: Principle behind the particle identification of the ARICH counter. [9]

## 1.6 $K_L^0$ and $\mu$ Detection (KLM)

The KLM is located outside the superconducting solenoid. It consists of alternating 4.7 cm thick iron plates and active detector elements. There are 15 detector layers and 14 iron plates in the barrel region and 14 detector layers and 14 iron plates in each endcap. The iron plates provide over 3.9 additional interaction lengths of material on top of the 0.8 provided by the ECL.

## 1.7 Detector Alignment

To reach an optimal detector performance it is necessary to know the exact physical parameters of the detector. In simulations, it is assumed that the detector perfectly corresponds to the design parameters. However, in reality, it is constructed with finite precision and some small deviations from the design are inevitable. The parameters may even change over time due to variations in temperature, weakening of material and many other factors. Therefore, trying to measure the detector is not reliable and the best way to determine the physical parameters of the detector is to utilize data collected by the detector itself [10]. With a sufficient statistical sample we can determine the real positions, rotations and deformations of the detector components and achieve much higher precision then by measuring them directly. This process of using data collected by the detector to parametrize it is usually referred to as alignment.

At Belle II the Millipede II tool is used to compute the detector parameters through minimization of track-to-hit residuals by means of a linear least squares method. Millipede fits all track and alignment parameters simultaneously and all correlations are kept in the solution. For this reason VXD and CDC are integrated into the system together [8].

While the alignment described above drastically improves the detector resolution, a non-random, systematic misalignment could introduce dangerous physics biases. Certain configurations can even produce seemingly valid tracks. In order to minimize such cases we will use particles from two completely different sources:

pairs of muons produced in collisions and muons from cosmic radiation. More on this topic will be discussed in chapter 2. And in chapters 3 and 4 we will study the correlations between track parameters to verify that no such bias is present in addition to also examining the general performance and precision of the detector.

# 2. Methodology

## 2.1 Particle Choice

We will use data collected by the detector to evaluate its performance. The core principle behind our method is to take two particles originating from a single interaction point (IP), then to reconstruct both trajectories and compare them at the IP where, under ideal circumstances, they should meet.

The best particles for this task are muons from $e^+e^- \to \mu^+\mu^-$ events. Both muons originate from the same IP and due to their relatively high mass of $\approx 105.7\,\mathrm{MeV}/c^2$ are less affected by multiple scattering than lighter particles such as electrons. Because muons are charged particles we can also easily calculate their momenta from the curvature of their tracks in the magnetic field inside the detector. They penetrate through material easily so we can detect muons from cosmic radiation passing through the detector. Although cosmic muons are quite rare they still provide a useful tool as they can be used to eliminate certain systematic errors in alignment. An example of such case is shown in Fig. 2.1.

Electrons from Bhabha scattering $e^+e^- \to e^+e^-$ would be another good candidate. However, they are more affected by multiple scattering than muons. And no electrons from cosmic radiation can reach the inner parts of the detector which eliminates the possibility to use cosmic radiation to study alignment. Therefore, we have chosen muons instead for the following analysis.

## 2.2 Track Reconstruction

The tracks have been reconstructed using the Belle II Analysis Software Framework (basf2) from raw data or mini data-summary table (mDST) files. (An mDST file contains a curated list of post-reconstruction dataobjects which are provided for analysis use.)

The tracks are parametrized in the Cartesian coordinate system where the $z$ axis passes through the center of the detector in the direction of the beampipe, the $x$ axis is in the horizontal direction and the $y$ axis is vertical. The tracks are reconstructed backwards from the hits in the detector to the point of closest approach (POCA) to the origin of the coordinate system. They are described by five helix parameters as shown in Fig. 2.2. The parameter $d_0$ is the signed distance of the POCA to the $z$ axis, $z_0$ is the $z$ coordinate of the POCA, $\phi_0$ is the angle between the track transverse momentum and the $x$ axis at the POCA and $\lambda$ is the so-called track dip angle, i.e. the angle of the track in the $s - z$ space where $s$ is the path length along the circular trajectory in the $x - y$ projection. We will be using the tangent of this angle $\tan\lambda$ to parametrize the tracks. And the last shown parameter is the radius $R$ of the track curvature in the $x-y$ plane. We will be using the inverse of this parameter $\omega = \frac{1}{R}$, the absolute value of the track curvature, from which the transverse momentum $p_t$ of the particle can be derived.

For cosmic rays the tracks are reconstructed as if they were two separate muons originating from the POCA instead of a single muon from outside the

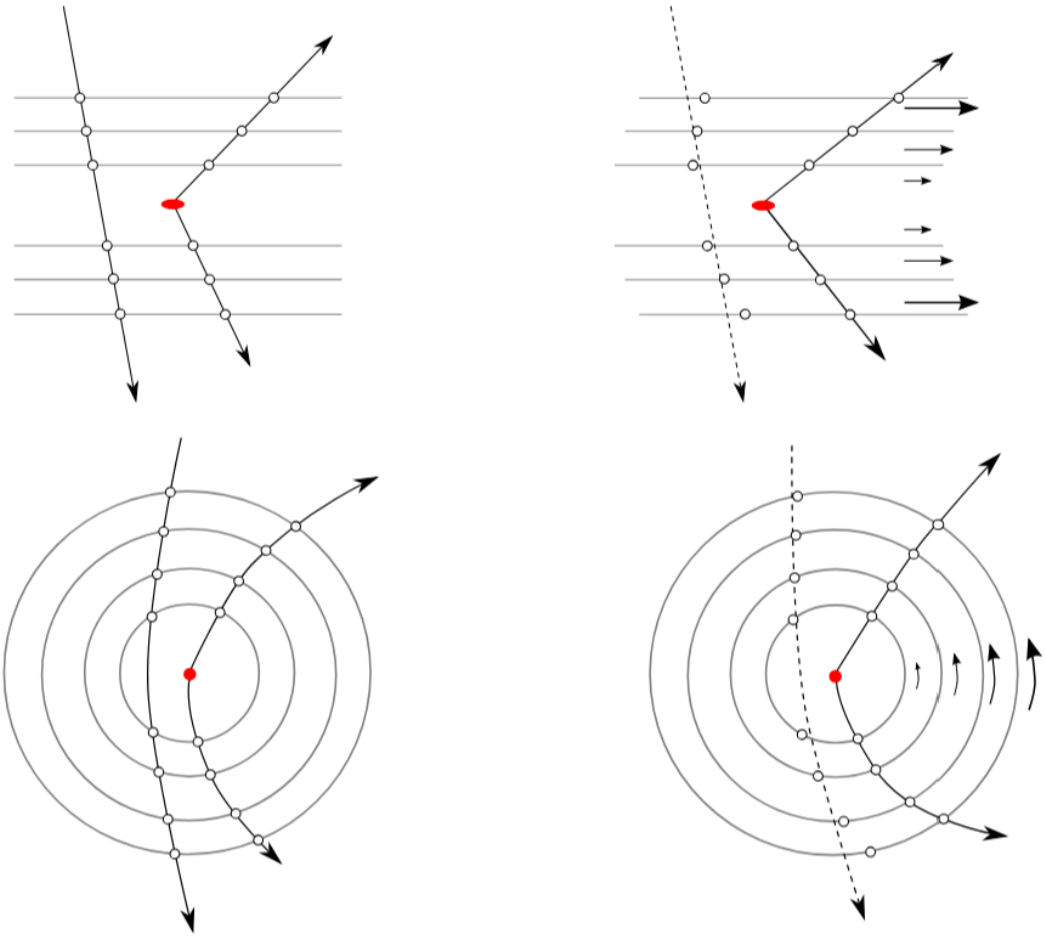

Figure 2.1: Illustration of two cases of misalignment (right) where data from cosmic rays can provide unique information. [10]

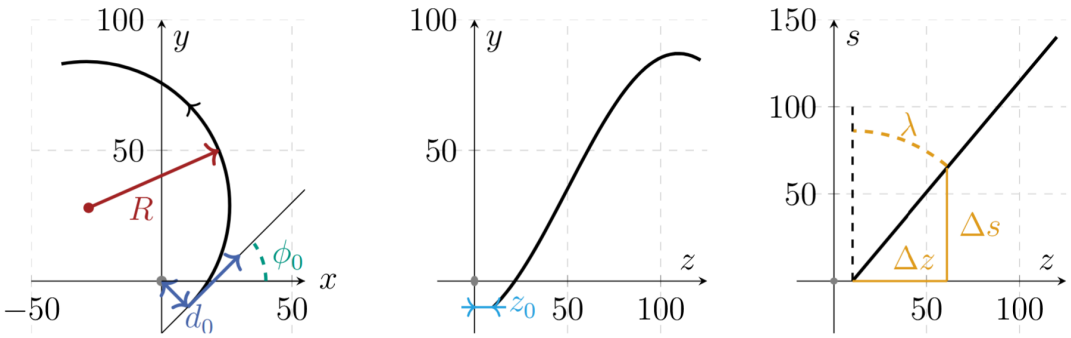


Figure 2.2: Schematic representation of a track and the track parameters describing it. [11]

detector. This way we can then compare the two tracks to study the accuracy of the reconstruction.

To compare the tracks we will use the difference of track parameters $\Delta h$, where $h$ is any helix parameter, that is defined as

$$\Delta h = \frac{h_1 - h_2}{\sqrt{2}} \tag{2.1}$$

Where $h_1$ is a helix parameter for the first track and $h_2$ is the one for the second.

For the studies of the detector performance using muons from cosmic radiation we will sometimes use the average of the helix parameters of the two tracks. This is done to more accurately represent the track that originates from a single particle unlike the tracks of muons from collisions.

$$\bar{h} = \frac{h_1 + h_2}{2} \tag{2.2}$$

# 3. Study of the Detector Performance Using Cosmic Radiation

The validation of the alignment using muons from cosmic rays has previously been done in [12]. However, there has been a unique opportunity, as up until now only the inner layer and two modules in the outer layer of the PXD have been installed, but now the PXD has been completed. Therefore, we can now evaluate the performance of the complete detector. In this chapter we will look at the data collected shortly after the PXD commissioning, while the magnetic field of the detector disabled.

We will look at two different reconstructions of data taken during this time, it is from experiment 28 runs 22 to 164. (That corresponds to the dates between 21.9.2023 and 2.10.2023.) The first one is with alignment applied and contains 4 925 314 events. It will be denoted as "nofield_alignment". The second is without any alignment and contains 6 620 021 events. It will be denoted as "nofield_noalignment". Both reconstructions were applied to the same dataset, so the difference in the number of events is only due to changes in reconstruction caused by the alignment.

## 3.1 First Look at the Data

First we will look at histograms of the different track parameters to understand the data better. All histograms have been normalized to reduce the effects of the different number of events between the two datasets. From the histograms in Fig. 3.1 we can see that the cosmic rays cover a very wide area. In fact, they pass through the entire detector (only 96 % of the data is shown in the histograms for better readability). The peaks in the middle of the histograms show areas where the parts of the detector with the optimal acceptance (detection efficiency) in the track parameter space.

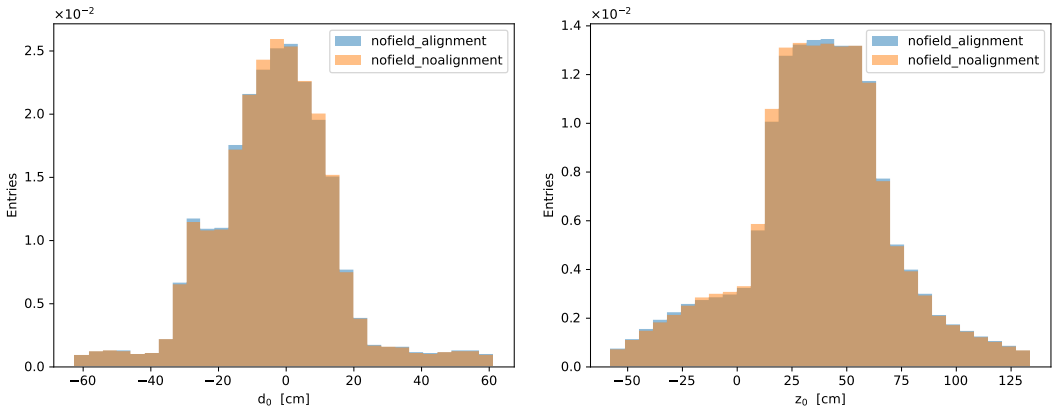


Figure 3.1: Histograms of the parameters $d_0$ (left) and $z_0$ (right) for all cosmics without any cuts.

However, we are only interested in the tracks passing through the vertex detector. Even more than that, we want to compare the results to muons from collisions in the next chapter. So we will only choose muons that pass through the beampipe area. That means we will use only tracks that fulfil

$$-1 < d_0 < 1; -2 < z_0 < 4 \tag{3.1}$$

After the beampipe cut 3.1 we are left with 4982 events for nofield_alignment and 6418 events for nofield_noalignment. That is a significant reduction, and we can already see the disadvantage of using cosmic muons: their low count. The histograms of $d_0$ and $z_0$ after the cut can be seen in Fig. 3.2. We can see that the parameters are now evenly distributed over the entire interval and there is no significant difference between nofield_alignment and nofield_noalignment, which is what we expected from cosmic radiation.

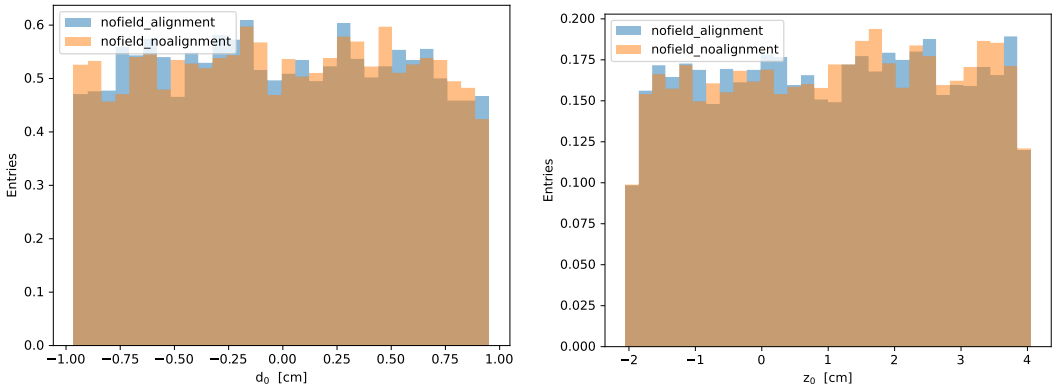


Figure 3.2: Histograms of the parameters $d_0$ (left) and $z_0$ (right) for cosmics with a beampipe cut (shown in equation 3.1).

The angular distributions are shown in Fig. 3.3. Most of the tracks are in the vertical direction ($\phi = -\frac{\pi}{2}\text{rad}; \tan\lambda = 0$). This is another disadvantage of cosmic tracks that we have not discussed yet. The least amount of material between the open sky and the detector, that the muons have to pass through, is in the vertical direction and quickly increases at different angles. As a result there are almost no horizontal cosmic tracks. This slightly limits our ability to study the detector evenly.

If we look at the track curvature $\omega$ in Fig. 3.4 we can see that without alignment the peak is much wider and not centered around zero. This means that the resolution is worse, and the tracks are on average more curved than in the data with alignment. However, we know that the magnetic field inside the detector is turned off, so the curvature we see must be non-physical. With good alignment all these effects are eliminated.

On the right side of Fig. 3.4 is a histogram of the transverse momentum $p_t$. This information is completely inaccurate since without any magnetic field there is no curvature of the tracks that would then be reconstructed as extremely high momenta which is what we see in Fig. 3.4. In Fig. A.1 we can see the typical momentum distribution for cosmics according to [12], so what we have measured is indeed incorrect. To determine the momenta of the muons accurately we would have to discard the information from the VXD and use only CDC and

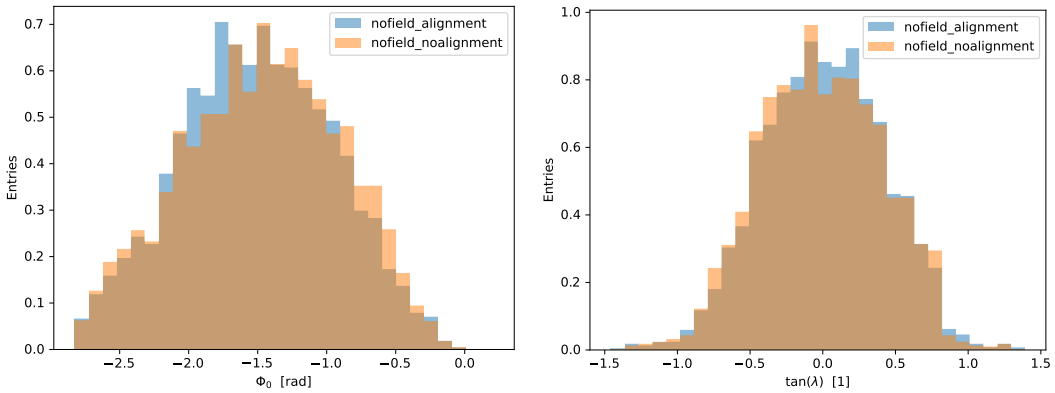


Figure 3.3: Histograms of the angles $\phi_0$ (left) and $\tan\lambda$ (right) for cosmics with a beampipe cut (shown in equation 3.1).

KLM. That would be outside the scope of this thesis as our main focus is on the Vertex Detector.

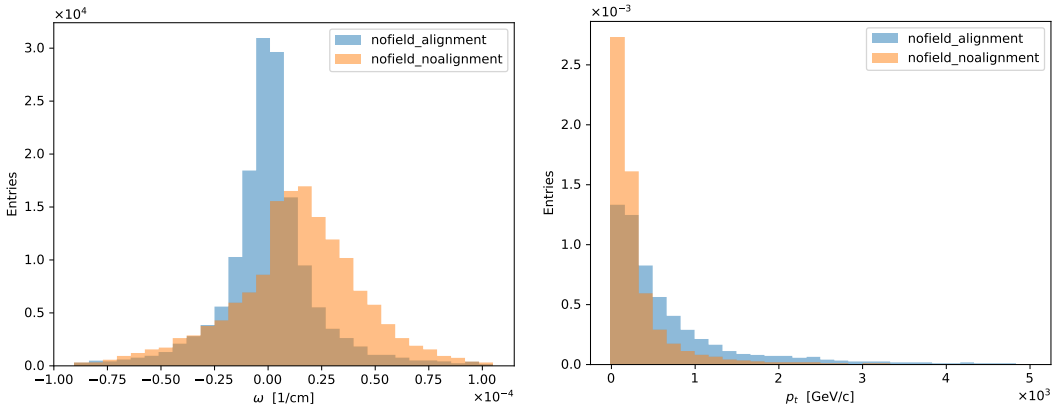


Figure 3.4: Histograms of the track curvature $\omega$ (left) and transverse momenta $p_t$ (right) for cosmics with a beampipe cut (shown in equation 3.1).

## 3.2 Correlations of Helix Parameters

Now we will look at correlations between the helix parameters that were briefly discussed in section 1.7. For an ideal detector, the differences of the track parameters obtained from the fit for both arms of the cosmic track should be normally distributed with a mean at zero and should not be a function of the track parameters. Therefore, all correlations we observe must be non-physical and caused by misalignment.

The correlations of the differences of the track parameters defined in 2.1 with the average of the parameters for the two tracks defined in 2.2 are plotted in the Fig. 3.5. The uncertainties $\sigma_{\Delta h}$ have been estimated as

$$\sigma_{\Delta h} = \sqrt{\frac{\sigma_i}{N_i}} \tag{3.2}$$

Where $\sigma_i$ is the standard deviation of the values within a single bin and $N_i$ is the number of events in that bin. In 3.5 we can see that the uncertainties are quite large, even in areas where we would expect good statistics and thus small uncertainties. To see if this hypothesis is correct we can look at a histogram showing the number of events in each bin. In Fig. 3.6 are 2D histograms for nofield_alignment and in Fig. 3.7 for nofield_noalignment. Brighter colors mean more events in a bin.

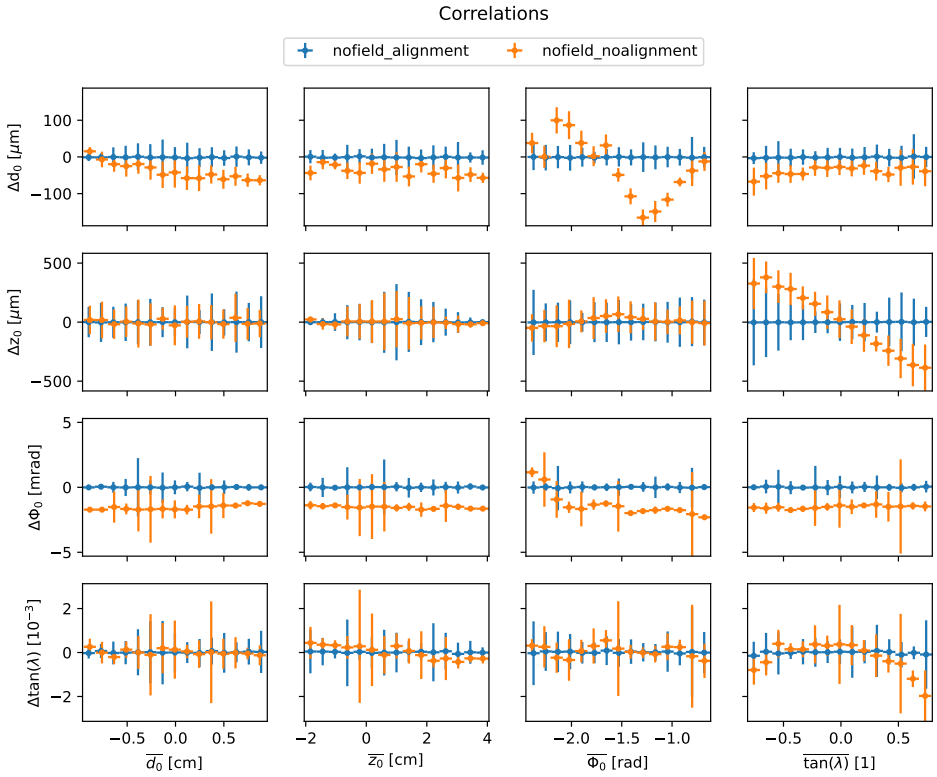


Figure 3.5: Correlations of the helix parameters for cosmic muons with the beampipe cut 3.1.

From the histograms we can clearly see that the errors are too big, especially from Fig. 3.6 it is clear that the errors are much larger than the width of the peaks. It is possible that a few outliers are causing the large uncertainties. We can remove them by performing the following selection

$$|\Delta d_0| < 2\,\text{mm}; |\Delta z_0| < 2\,\text{mm} \tag{3.3}$$

The correlations after this cut can be seen in Fig. 3.8. The uncertainties have been reduced dramatically while the correlations themselves did not change. After this cut there are 4737 events in nofield_alignment and 6115 in nofield_noalignment. By performing this cut we have removed approximately 5 % of the data.

Now we can finally discuss the correlations themselves. The results are not surprising, without alignment there are various non-physical correlations in most of the parameters, but with alignment at this scale are no visible correlations. That is a promising result.

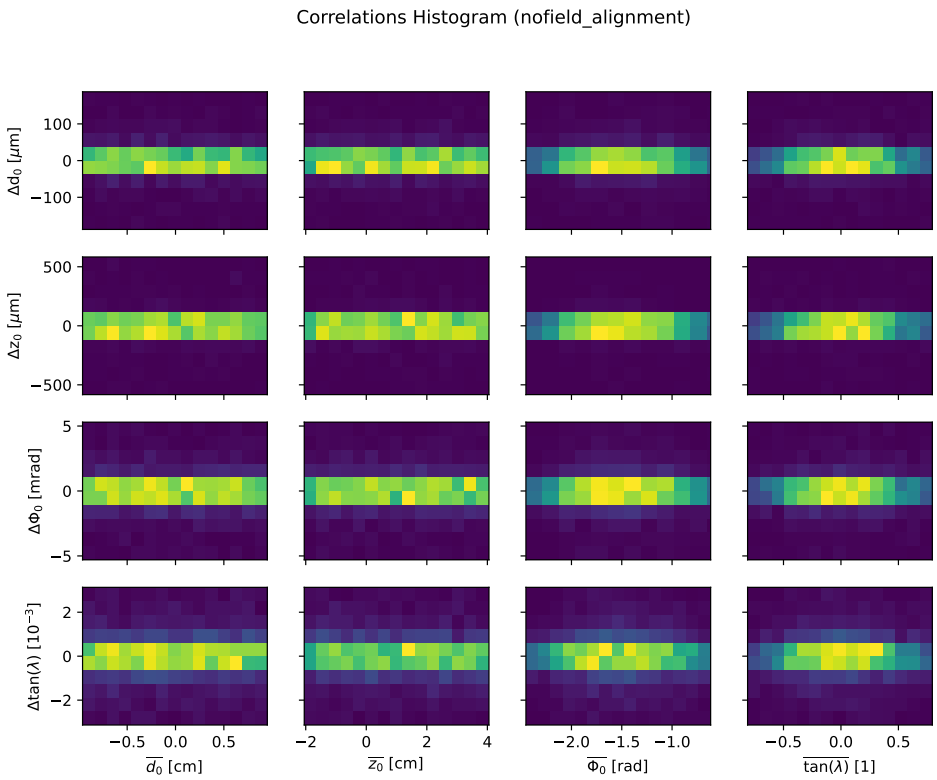


Figure 3.6: Histogram of correlations of the helix parameters for cosmic muons with alignment with the beampipe cut 3.1. Lighter colors signify larger number of events.

In greater detail correlations for the cosmic muons with alignment (nofield_alignment) are shown in Fig. 3.9. We can see that all the correlations are zero within uncertainties. Thus, we can safely conclude that there are no non-physical correlations between the parameters that can be observed using cosmic radiation.

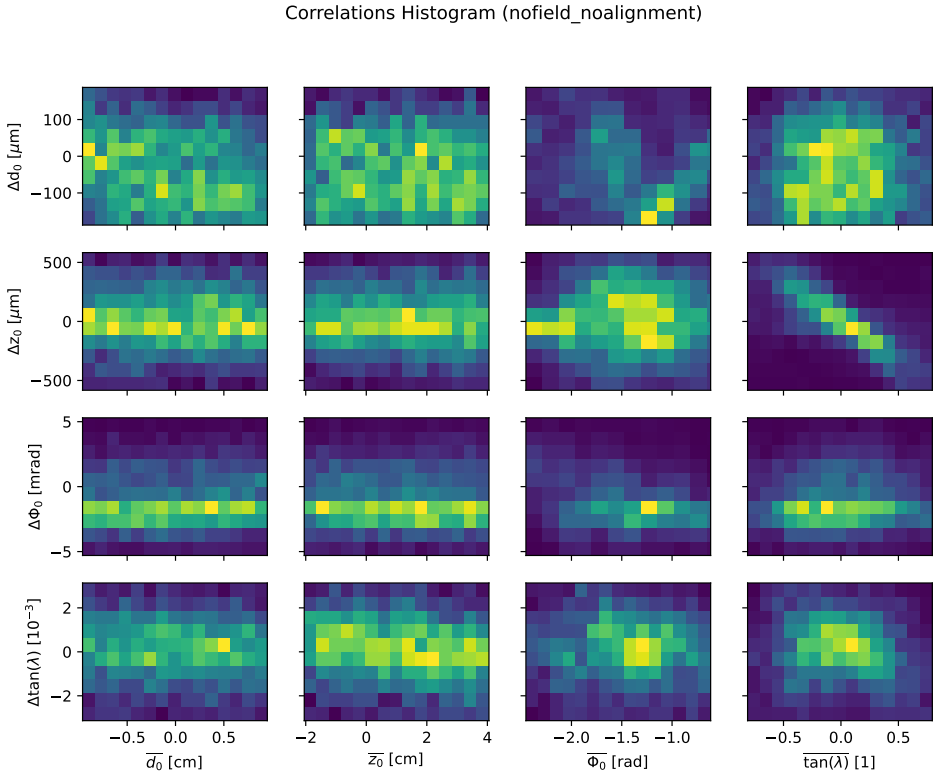


Figure 3.7: Histogram of correlations of the helix parameters for cosmic muons without alignment with the beampipe cut 3.1. Lighter colors signify larger number of events.

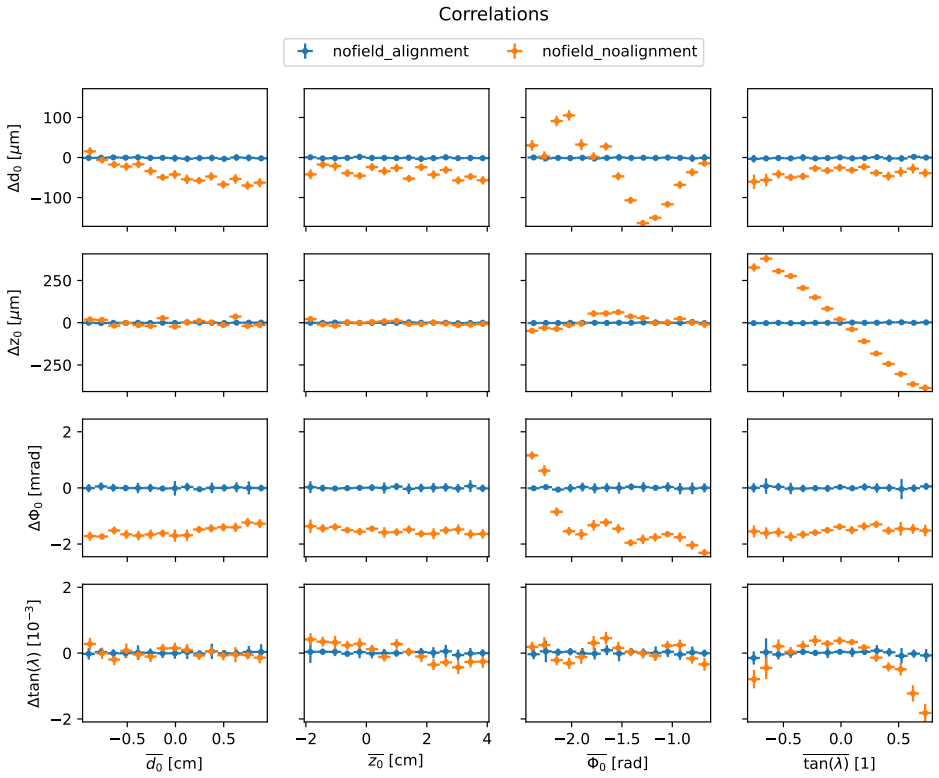


Figure 3.8: Correlations of the helix parameters for cosmic muons with the beampipe 3.1 and outlier 3.3 cuts.

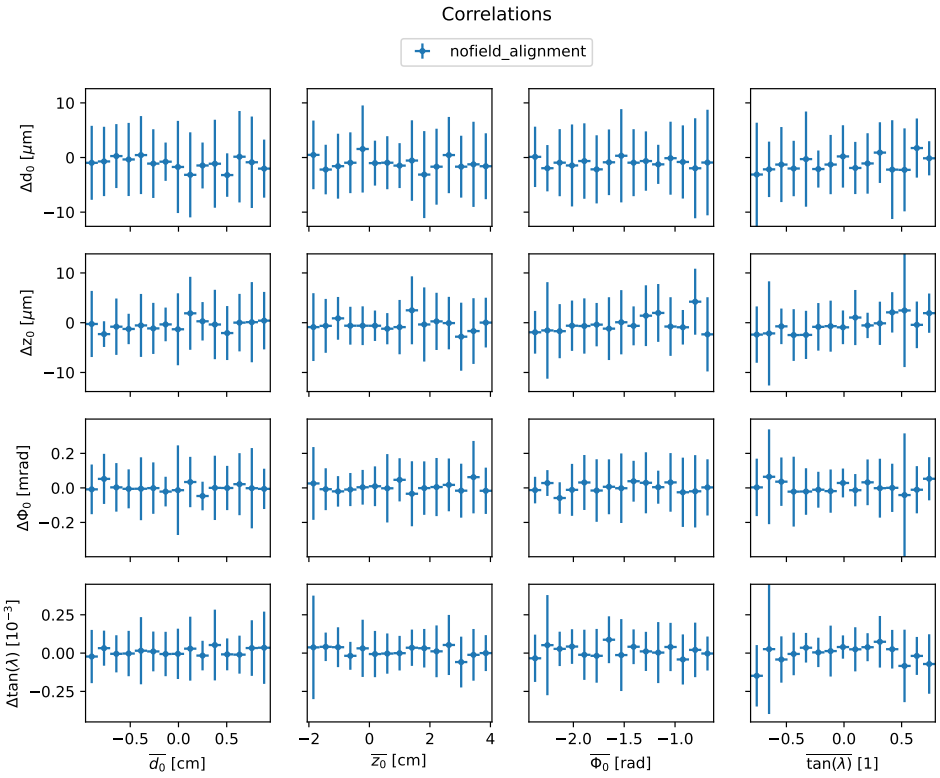


Figure 3.9: Correlations of the helix parameters for cosmic muons with the beampipe 3.1 and outlier 3.3 cuts. Detail on nofield_alignment.

## 3.3 Resolutions

Now comes the last and most important step of the study of the performance of the Vertex Detector using cosmic muons. It is to determine the resolution of the detector. In [12] it has been shown that the resolution depends on the momenta of the particles. However, due to the magnetic field inside the detector being disabled for this data we have no reliable information about the momenta. Thus, our only option is to determine the average resolution over the entire range of momenta of all the muons from cosmic radiation.

The resolutions are shown in Fig. 3.10. These plots have been normalized to compare the two datasets with different number of events. Again 96 % of the total data is shown for each dataset, and they are both binned independently to keep a high amount of detail.

The resolution $\sigma_{68}$ has been determined as the width of a one sigma interval, i.e. interval containing 68 % of the data. Also, the median has been calculated to reveal any possible bias in the data that could hint at a non-statistical systematic error. Median has been used instead of a mean because it is more stable and less affected by outliers, which we have shown are present in the data.

These plots are some of the best examples of how important good alignment is. The resolution is improved by an entire order of magnitude and various non-physical effects and biases are completely removed. However, we can see that even after alignment there is still as slight bias of $-1\,\mu\text{m}$ in $\Delta d_0$. A similar bias has also been observer in [12] even in Monte Carlo simulation. But in simulations a perfect alignment is assumed, so this must be caused by something different and completely independent of alignment.

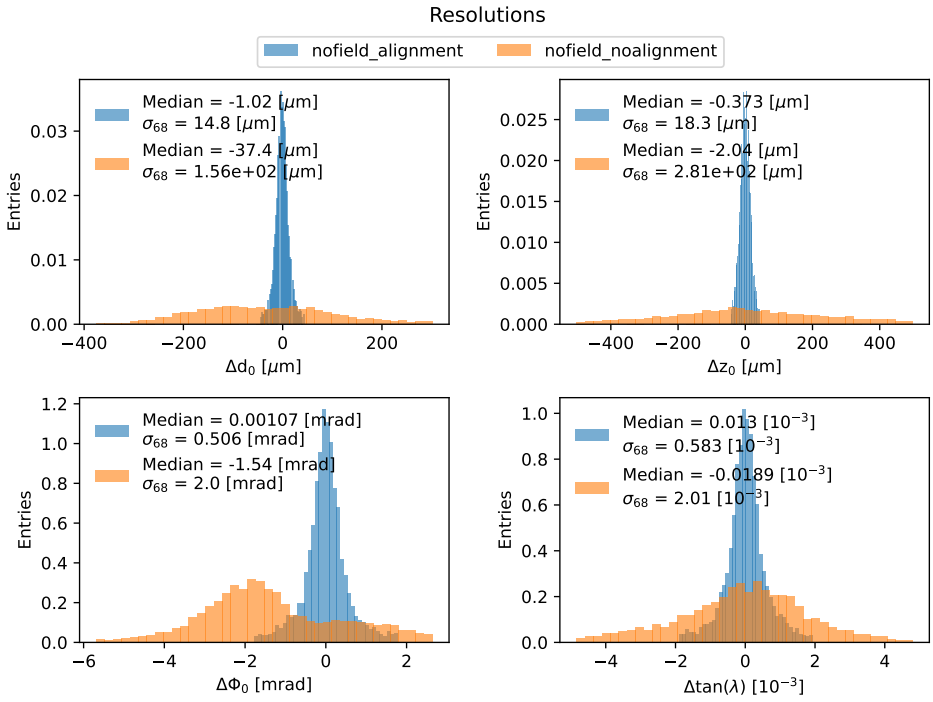


Figure 3.10: Resolution of the four helix parameters $d_0$, $z_0$, $\phi_0$ and $\tan\lambda$ for data with both the beampipe 3.1 and 3.3 outlier cuts.

We have determined the resolutions by measuring the width of the $\sigma_{68}$ interval. However, this method does not provide any information about the uncertainty of the width determined in this way. Finding the uncertainty of $\sigma_{68}$ would require the use of advanced statistical methods such as bootstrap resampling. Instead, we have decided to perform a Gaussian fit to determine $\sigma$ and its uncertainty.

The exact form of the distribution used to fit the data is the following

$$f(x) = \frac{a}{\sqrt{2\pi\sigma^2}} e^{-\frac{(x-\mu)^2}{2\sigma^2}} \tag{3.4}$$

Where $a$, $\sigma$ and $\mu$ are parameters of the fit.

The helix parameters $\Delta\omega$ and $\frac{\Delta P_t}{P_t}$ are shown for completeness but should not be considered as real results. Due to the disabled magnetic field the measured values are meaningless.

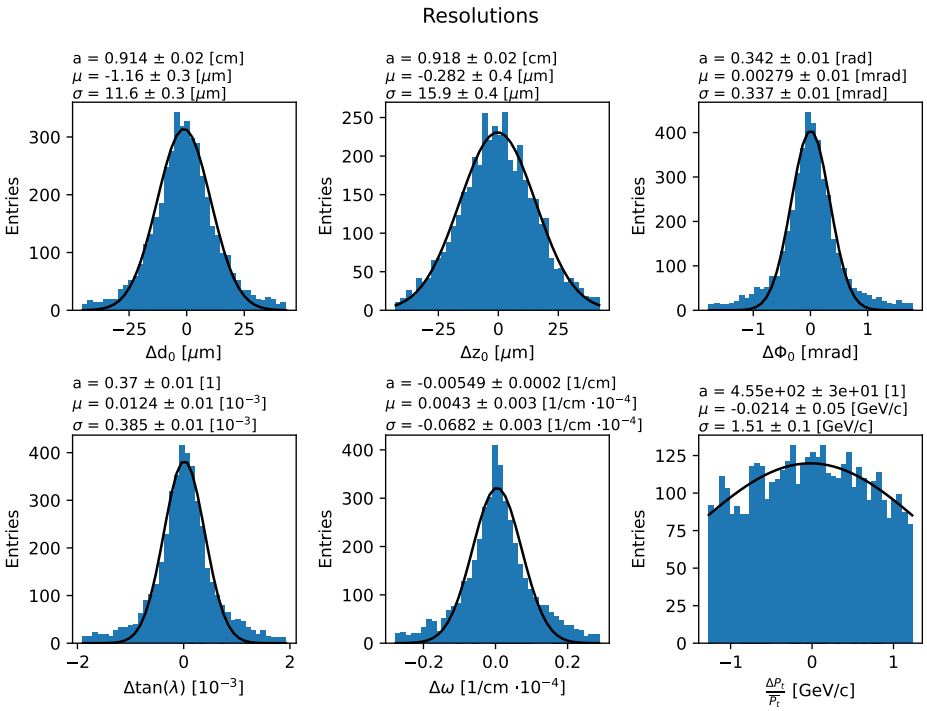


Figure 3.11: Histograms of the helix parameters fitted with a Gaussian distribution 3.4 to approximate the resolution of the detector.

If we compare Fig. 3.10 and Fig. 3.11 we can see that by performing a fit over the entire dataset we were able to obtain slightly better resolutions. The results of the fit can also be found in table 3.1.

Table 3.1: Resolutions of the helix parameters using muons from cosmic radiation.

| Helix parameters | $\mu$ | $\sigma$ | $\frac{\lvert\mu\rvert}{\sigma}$ [%] |
|---|---|---|---|
| $d_0$ [µm] | -1.2 ± 0.3 | 11.6 ± 0.3 | 10.3 ± 2.6 |
| $z_0$ [µm] | -0.3 ± 0.4 | 15.9 ± 0.4 | 1.8 ± 2.5 |
| $\phi_0$ [rad] | 0.00 ± 0.01 | 0.34 ± 0.01 | 0.8 ± 2.9 |
| $\tan\lambda$ [$10^{-3}$] | 0.01 ± 0.01 | 0.39 ± 0.01 | 2.5± 2.5 |

# 4. Study of the Detector Performance Using $e^+e^- \to \mu^+\mu^-$ Events

In this chapter we will use the data from $e^+e^- \to \mu^+\mu^-$ events to study the detector. First we will use a Monte Carlo simulation (MC) to better understand the data without any disruptive effects such as misalignment. We will then compare it with recent data collected in 2024. The point of closest approach (POCA) is defined with respect to the interaction point (IP) instead of the point of origin for data from collisions.

The data were taken from a tight di-muon skim which provides a clean sample containing mostly muons and electrons. During the reconstruction/simulation only events with exactly two tracks were then selected. In addition, the following requirements were applied:

$$p > 1\,\mathrm{GeV}/c; |z_0| < 2\,\mathrm{cm}; d_0 < 0.5\,\mathrm{cm}; 9.5\,\mathrm{GeV}/c^2 < M < 11\,\mathrm{GeV}/c^2 \qquad (4.1)$$

Where $p$ is the momentum of each muon and $M$ is the reconstructed invariant mass of the muon pair. Then, in our analysis, only events with a muon identification probability greater than 80 % were accepted. This probability is determined using information from all available detectors.

## 4.1 Simulation

Let us now look at the data from the Monte Carlo simulation. They will be denoted simply as 'MC'. After applying all the selections mentioned above we are left with 282 149 events.

### 4.1.1 First Look at the Data

First, we can examine how the muons are distributed throughout the detector, to confirm our statements in section 2.1. We will achieve this by making a 2D histogram of the tracks where each bin represents a small section of the detector. This can be seen in Fig. 4.1, where lighter colors represent bins with a higher number of events.

As we can see, our claims were correct, and the muons cover the entire detector. The two dark spots at approximately $\phi_0 \approx 1.5\,\mathrm{rad} \times \tan\lambda \approx 0.5$ and $\phi_0 \approx -1.5\,\mathrm{rad} \times \tan\lambda \approx 1.5$ are areas where electrons and positrons from Bhabha scattering, removed by our selection, predominantly pass through. Such a histogram would not be possible for cosmic muons which we presented in chapter 3 due to their low count.

Now we can examine individual histograms of the helix parameters to understand the data. In Fig. 4.2 we can see that the unlike cosmic rays the tracks are distributed in a small area around the interaction point.

The angles $\phi_0$ and $\tan\lambda$ are shown in Fig. 4.3. The parameter $\phi_0$ is distributed mostly evenly across the entire range. There are four slightly preferred angles of

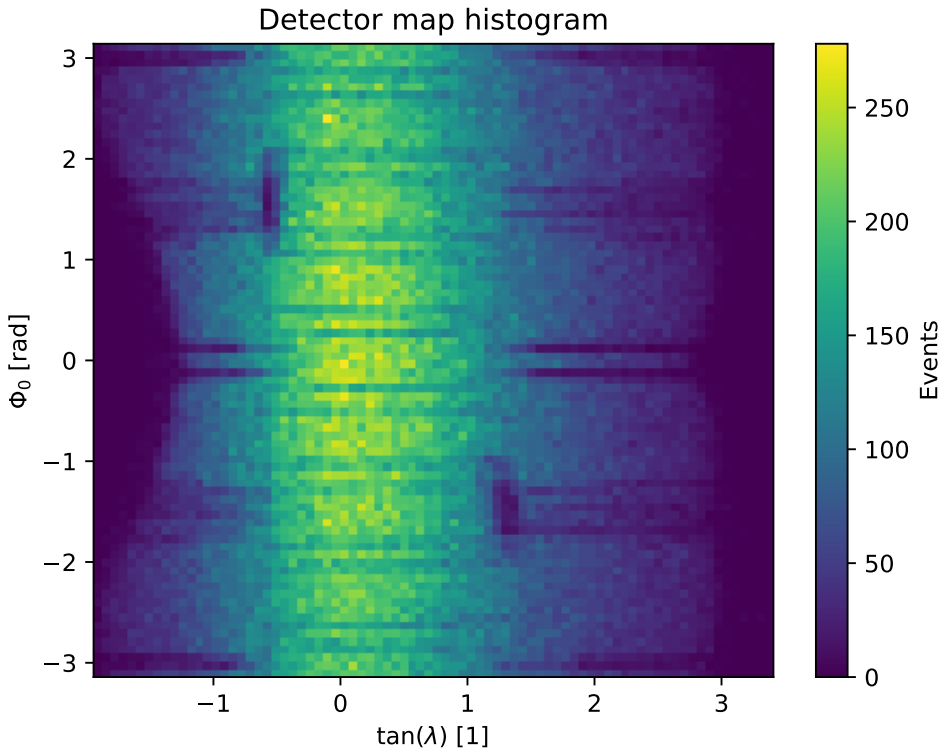


Figure 4.1: A 2D histogram of all muons from collisions (MC).

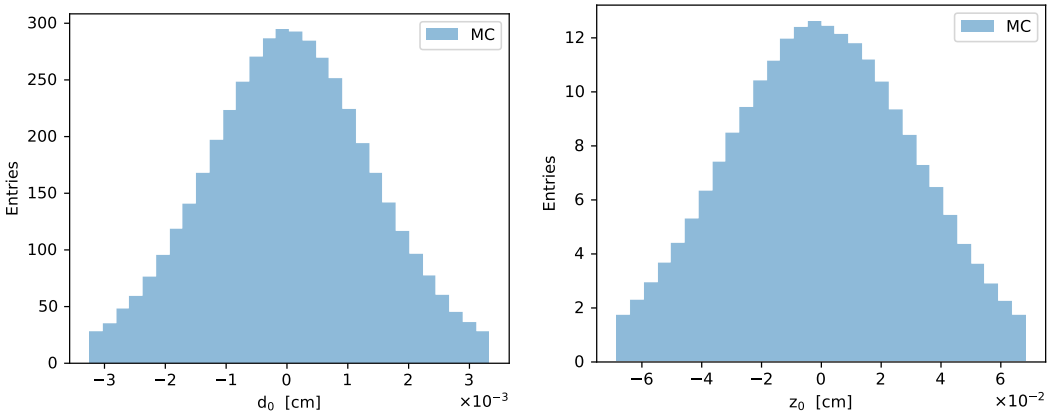


Figure 4.2: Histograms of the parameters $d_0$ (left) and $z_0$ (right) for the MC.

$\pm\frac{1}{4}\pi$ and $\pm\frac{3}{4}\pi$. However, the difference is small and can be neglected for our purposes. And from the histogram of $\tan\lambda$ we can see that most of the tracks are in the forward direction, which is due to the boost to the CMS from the asymmetric energies of the colliding electrons and positrons discussed in chapter 1.

Finally, in Fig. 4.4 we can see histograms of the track curvature $\omega$ and the transverse momentum $p_t$. Due to $\mu^+$ and $\mu^-$ having opposite charges the curvature $\omega$ can be both positive or negative. The wide gap in the central section around 0 is caused by the finite energies of the electrons and positrons produced by the accelerator (higher momenta = smaller curvature). The distribution of

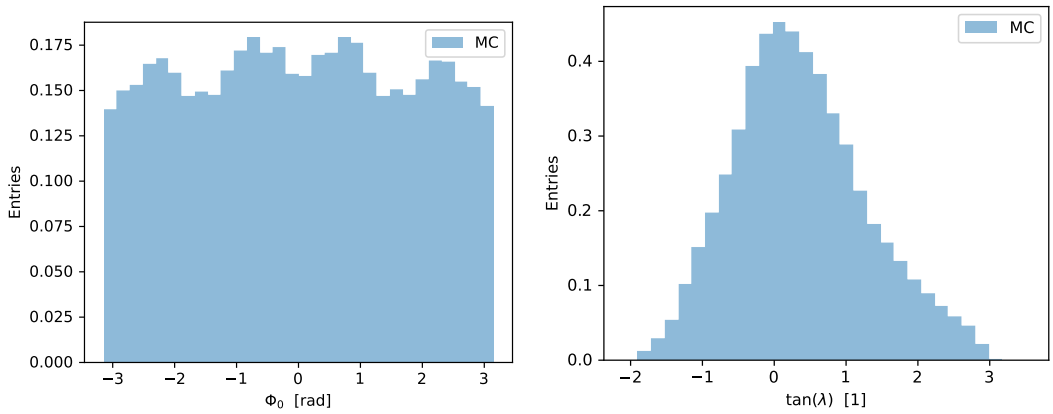


Figure 4.3: Histograms of the parameters $\phi_0$ (left) and $\tan\lambda$ (right) for the MC.

the transverse momenta $p_t$ follows from the kinematics of the process where momentum and energy has to be conserved.

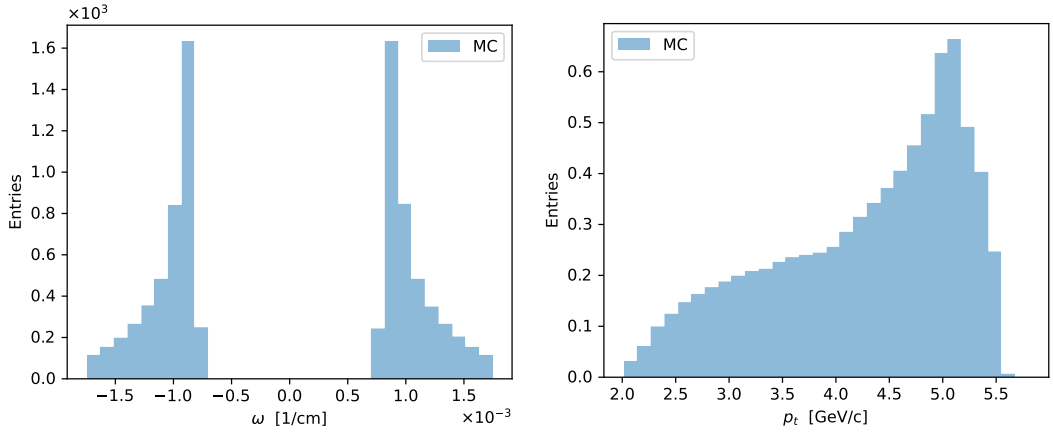


Figure 4.4: Histograms of the parameters $\omega$ (left) and $p_t$ (right) for the MC.

### 4.1.2 Correlations of Helix Parameters

Let us now look at the correlations of the helix parameters. Due to the forward boost given by the asymmetric energies of the electrons and positrons, the two tracks aren't exactly in the opposite directions. Therefore, the difference between the tracks in the angles $\phi_0$ and $\tan\lambda$ is not zero. As a result, we can only apply the method that was used for the cosmic muons in Fig. 3.8 to the parameters $d_0$ and $z_0$.

However, as was mentioned in chapter 2 $d_0$ is the **signed** distance of the POCA from the $z$ axis. This means that for the $\mu^+$, $\mu^-$ going in two directions the signs will be opposite. Therefore, instead of $\Delta d_0$ as defined in 2.1 we will use

$$\Sigma d_0 = \frac{d_{0_1} + d_{0_2}}{\sqrt{2}} \tag{4.2}$$

The correlations can be seen in Fig. 4.5 and their histograms in Fig. 4.6. The parameters shown are not correlated in any way, as was expected for a

simmulation where perfect alignment is assumed. The correlations of $\Delta\phi$ and $\Delta \tan\lambda$ are not shown, because as was discussed earlier the tracks do not have to be directly opposite to eachother and therefore $\Delta\phi$ and $\Delta \tan\lambda$ are not zero.

The plots $\Sigma d_0$ vs $d_0$ and $\Delta z$ vs $z_0$ are not shown because based on our definition of the parameters $d_0$ and $z_0$ any tracks that are not around zero are poor quality. In Fig. 4.2 we can see that most tracks are distributed very closely around zero.

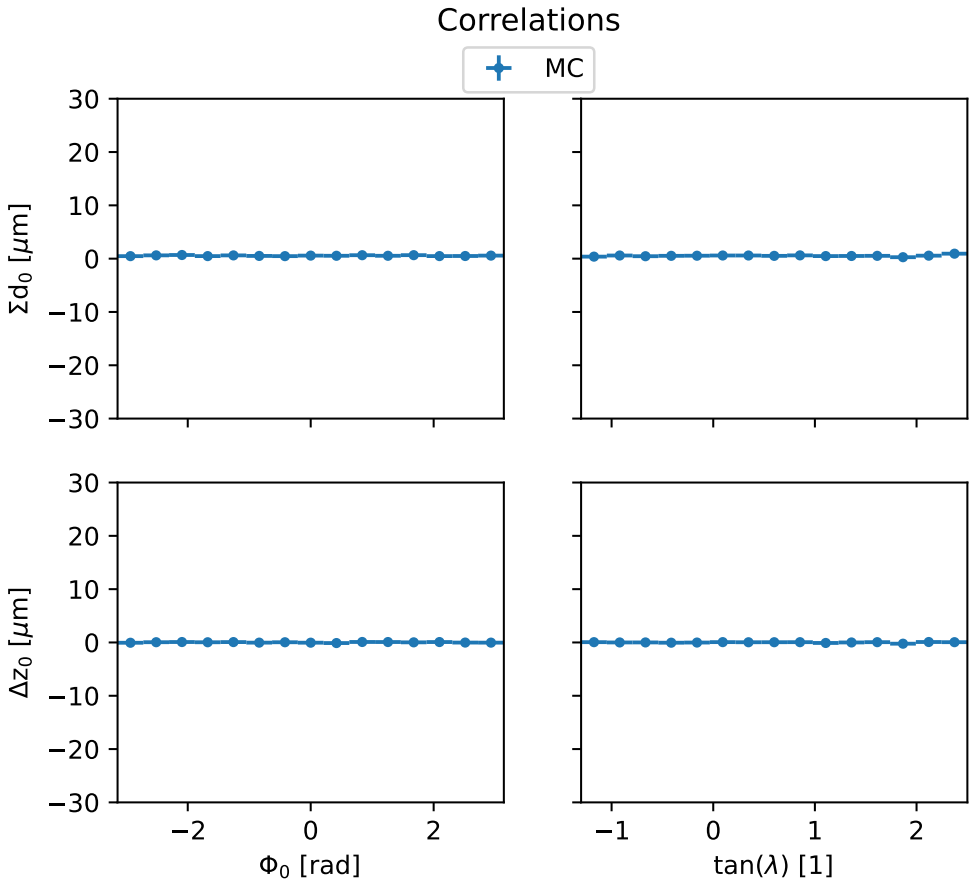


Figure 4.5: Correlations of the helix parameters for the MC.

As a note, the range of $-30\,\mu m$ to $30\,\mu m$ in Fig. 4.5 was chosen approximately as a double of the detector resolution. However, if we reduce the scale we can see a constant bias of approximately $0.5\,\mu m$. This is shown in Fig. A.3. This is well past the resolution of the detector and therefore not significant, but it resembles the bias in $d_0$ that was previously observed for cosmic muons both in data and simulations. However, due to the bias being so small, finding its cause is a low priority.

### 4.1.3 Resolutions

In this subsection we will examine the resolution of the detector. The resolutions are calculated as the half of the width of a one sigma interval, i.e. the interval containing 68 % of the data. In this chapter only the resolutions of the parameters $d_0$ and $z_0$ are shown. The resolutions of the parameters $\phi_0$ and $\tan\lambda$ are not calculated for the same reasons as their correlations were not shown in section

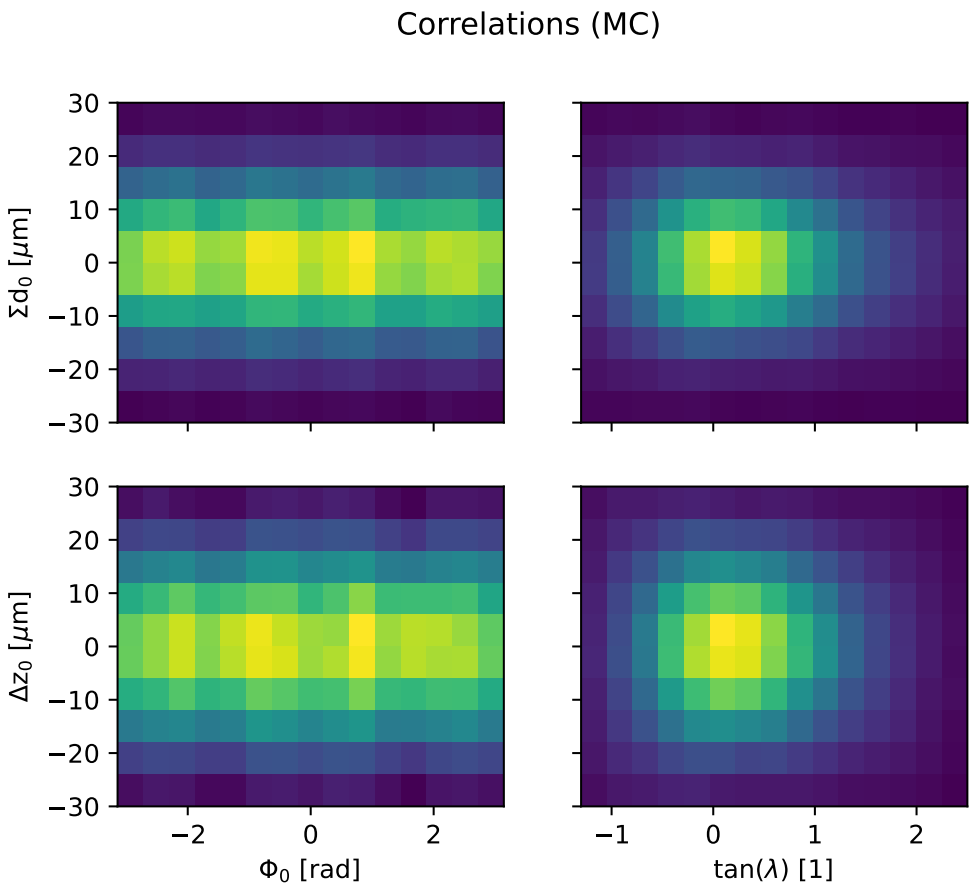


Figure 4.6: Histogram of correlations of the helix parameters for the MC.

4.1.2. This information can already be easily obtained using muons from cosmic radiation.

We will start by examining the detector for any areas which perform worse than the rest. To do so, we can plot the resolution with respect to the angles $\phi_0$ and $\tan\lambda$. The resolution of the parameter $d_0$ is shown in Fig. 4.7 and for $z_0$ in Fig. 4.8.

The best resolution is for tracks with $0 < \tan\lambda < 1$. This corresponds to muons passing through the main part of the detector and travelling almost perpendicular to the modules of the VXD. At this angle the muons pass through the least amount of material and are therefore least affected by multiple scattering.

The resolution remains mostly constant with respect to the $\phi_0$ angle. The only exceptions are faint periodic stripes of slightly reduced resolution. These are most easily seen in Fig. 4.8. There are eight 'stripes' that are the most visible. This would correspond to the structure of the inner layer of either the PXD or the SVD. Both have eight flat segments arranged in a circle around the beampipe. The areas where the individual modules overlap and the support structures on their edges contribute to the multiple scattering of the particles.

Figures 4.7 and 4.8 have given us a qualitative understanding of how the resolution changes with the angles. They show a lot of detail but are quite noisy and don't provide any uncertainties. To obtain a more quantitative understanding of how the resolution changes with the various helix parameters we can draw a sim-

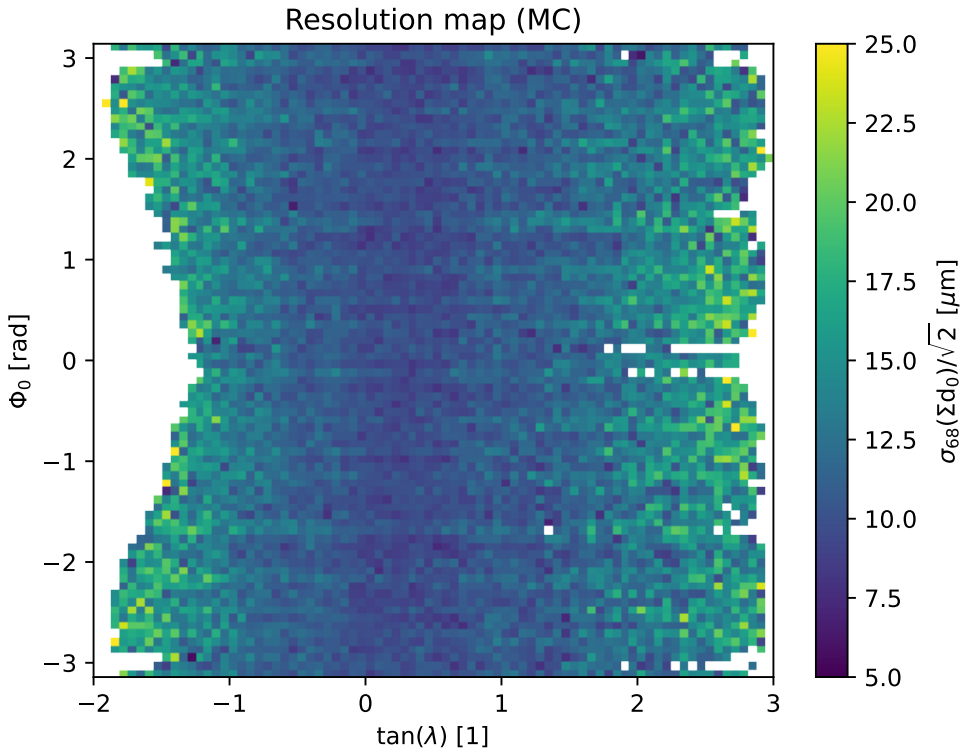


Figure 4.7: A map of the resolution of the helix parameter $d_0$ for the MC.

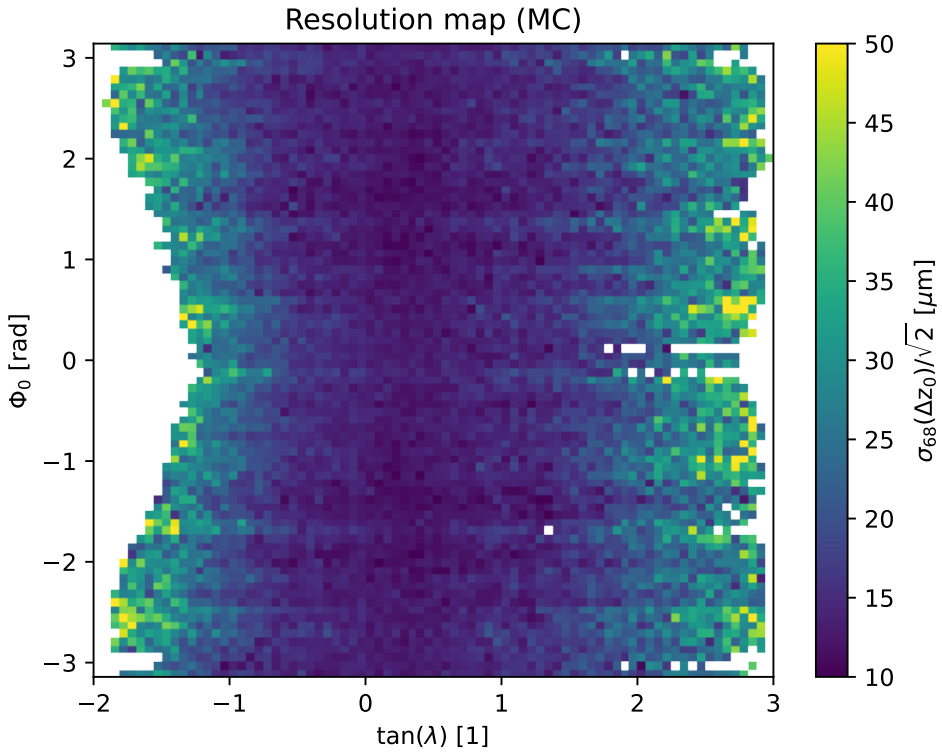


Figure 4.8: A map of the resolution of the helix parameter $z_0$ for the MC.

ilar plot to Fig. 4.5 but with resolutions instead of track parameters differences. This is shown in Fig. 4.9. The uncertainties have been approximated as 3.2.

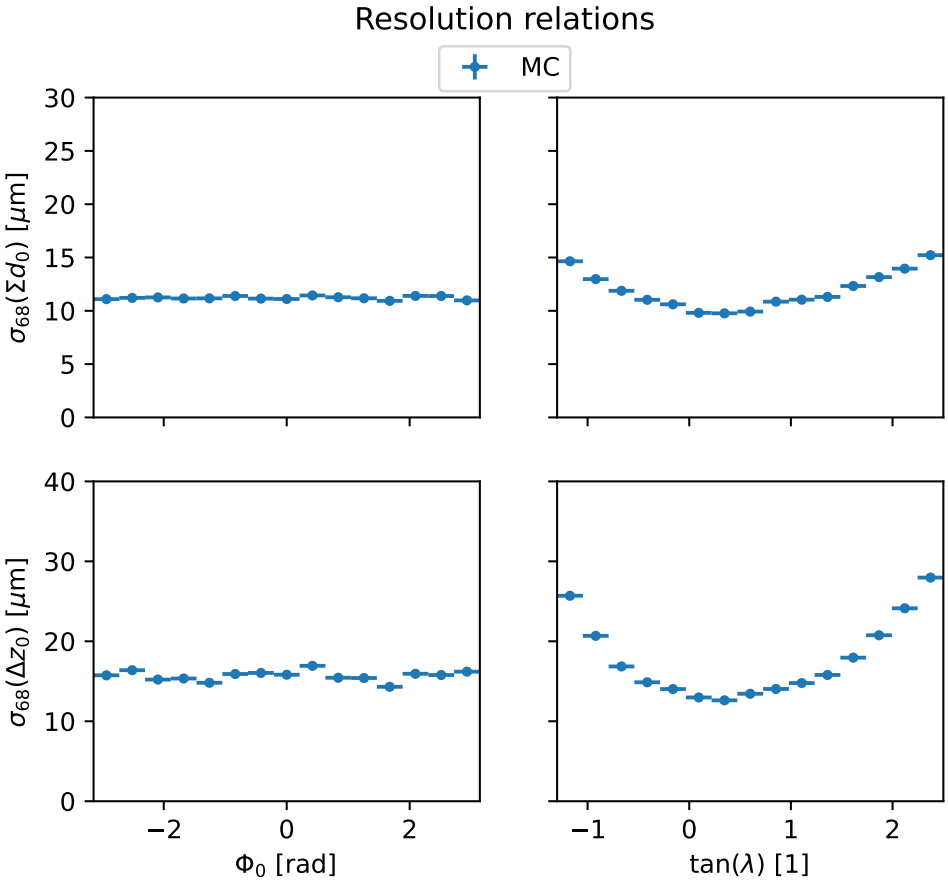


Figure 4.9: Resolutions of $d_0$ and $z_0$ with respect to the helix parameters.

Once again we can see that the resolution is heavily dependent on the angle $\tan\lambda$, the reasons for this behavior have been explained above. There is no dependence on angle $\phi_0$, that confirms what could be seen in Fig. 4.7 and Fig. 4.8.

In chapter 3 we have stated that the resolutions depend on the momenta of the particles due to the effects of multiple scattering. In this section have also shown that it is heavily dependent on the parameter $\tan\lambda$. Now we will combine the two parameters by defining so called pseudomomentum. For $d_0$ it is defined as

$$\tilde{p}_{d_0} = p\beta\sin(\theta)^{\frac{3}{2}} \tag{4.3}$$

and for $z_0$ as

$$\tilde{p}_{z_0} = p\beta\sin(\theta)^{\frac{5}{2}} \tag{4.4}$$

These values can be then calculated from the transverse momentum $p_\mathrm{T}$ and $\tan\lambda$. For simplicity, we will assume that the detector is a perfect cylinder and neglect the slanted modules in the front.

$$\tilde{p}_{d_0} = p_\mathrm{T}\sqrt{1+\tan(\lambda)^2}\,\frac{1}{\sqrt{1+\frac{0.105^2}{p_\mathrm{T}^2(1+\tan(\lambda)^2)}}}\,\frac{1}{(1+\tan(\lambda)^2)^{\frac{3}{2}}} \tag{4.5}$$

and for $z_0$ as

$$\tilde{p}_{z_0} = p_{\mathrm{T}}\sqrt{1+\tan(\lambda)^2}\frac{1}{\sqrt{1+\frac{0.105^2}{p_{\mathrm{T}}^2(1+\tan(\lambda)^2)}}}\frac{1}{(1+\tan(\lambda)^2)^{\frac{5}{2}}} \tag{4.6}$$

Equations 4.5 and 4.6 are shown in an expanded form to make identification of the corresponding elements in equations 4.3 and 4.4 easier.

Resolutions with respect to pseudomomentum are shown in Fig. 4.10. A finer binning was chosen in the interval $4\,\mathrm{GeV}/c < \tilde{p} < 5\,\mathrm{GeV}/c$ to better reflect the higher number of tracks in this interval that can be seen in Fig. 3.4. The bins are: $2\,\mathrm{GeV}/c$, $2.5\,\mathrm{GeV}/c$, $3\,\mathrm{GeV}/c$, $3.5\,\mathrm{GeV}/c$, $4\,\mathrm{GeV}/c$, $4.2\,\mathrm{GeV}/c$, $4.4\,\mathrm{GeV}/c$, $4.6\,\mathrm{GeV}/c$, $4.8\,\mathrm{GeV}/c$ and $5\,\mathrm{GeV}/c$. The range of the momenta available is smaller than for cosmic muons, but the statistics in each bin are better. The statistical uncertainties have been determined as the standard deviation of 100 bootstrap replicas (with replacement) of the data set.

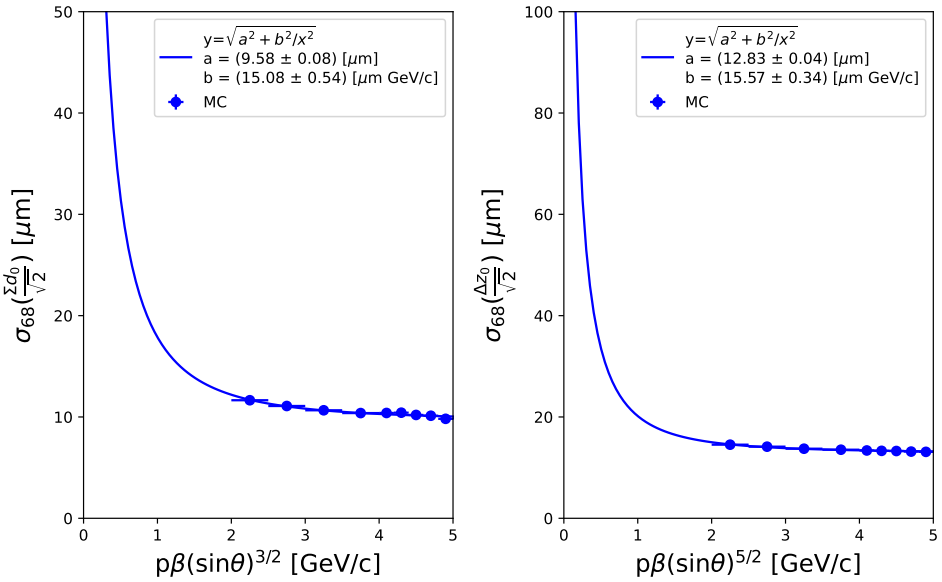


Figure 4.10: Resolutions of $d_0$ and $z_0$ with respect to pseudomomentum.

The points have then been fitted with the function 4.7 using the least squares method.

$$\sigma_{68}^2 = a^2 + \frac{b^2}{\tilde{p}^2} \tag{4.7}$$

The parameter $a$ corresponds to the resolution in an infinite momentum limit and the parameter $b$ parametrizes the effect of multiple scattering at lower energies.

The results of the fit for $d_0$ are:

$$a = (9.58 \pm 0.08)\mu\mathrm{m}$$

$$b = (15.08 \pm 0.54)\mu\mathrm{m}\,\mathrm{GeV}/c$$

And for $z_0$:

$$a = (12.83 \pm 0.04)\mu\mathrm{m}$$

$$b = (15.57 \pm 0.34)\mu\mathrm{m}\,\mathrm{GeV}/c$$

## 4.2 Data From Collisions

In this section we will use the data from $e^+e^- \to \mu^+\mu^-$ events collected during the year 2024 and compare it to the Monte Carlo simulation shown in section 4.1. The data was specifically from experiment 30 runs 3490 to 3502, that is between 29.4.2024 and 30.4.2024. After applying the selections described in section 4.1 there are 167 014 events. The data will be denoted as 'runs3490-3502'.

### 4.2.1 First Look at the Data

The distribution of the tracks throughout the detector is the same as for the MC and can be found in Fig. A.2.

The histograms of the parameters $d_0$ and $z_0$ in Fig. 4.11, $\phi_0$ and $\tan\lambda$ in Fig. 4.12 and $\omega$ and $p_\mathrm{T}$ in Fig. 4.13 have been normalized to allow for comparison of two datasets of different size. The measured data corresponds to the simulation almost perfectly. The small differences that are visible can be attributed to statistical fluctuations.

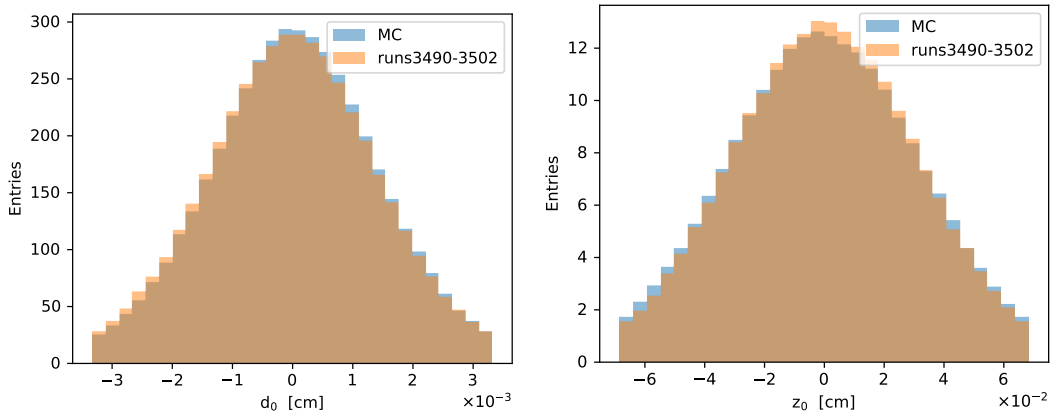


Figure 4.11: Histograms of the parameters $d_0$ (left) and $z_0$ (right) for muons from collisions.

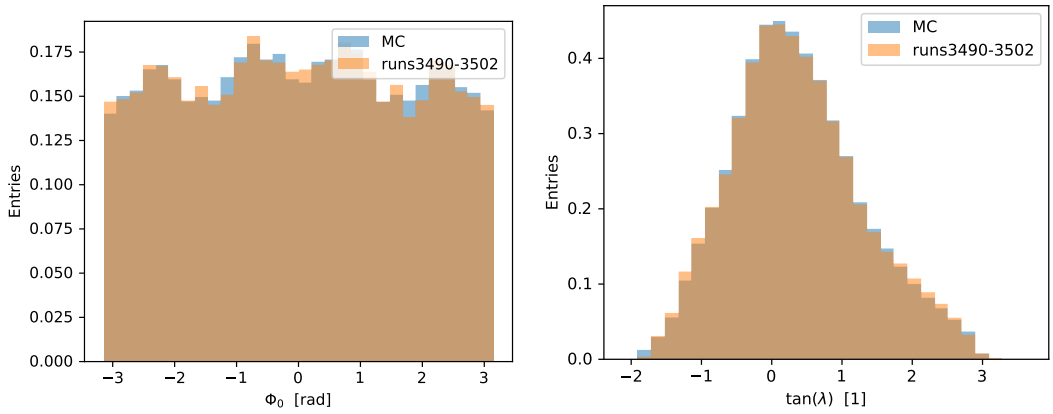


Figure 4.12: Histograms of the parameters $\phi_0$ (left) and $\tan\lambda$ (right) for muons from collisions.

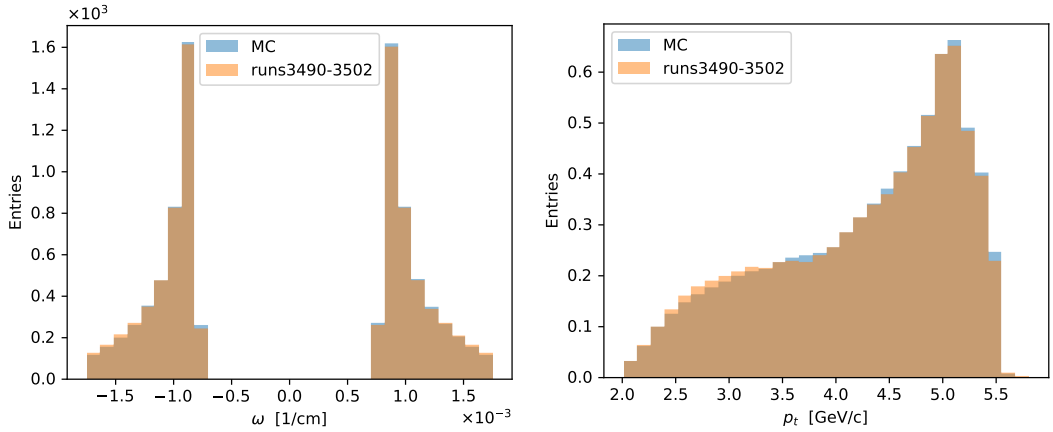


Figure 4.13: Histograms of the parameters $\omega$ (left) and $p_t$ (right) for muons from collisions.

### 4.2.2 Correlations of Helix Parameters

The correlations of the helix parameters are compared with the MC in Fig. 4.14. At this scale the data does not deviate from the simulation. Only if we look at a scale smaller than the resolution of the detector can any difference be seen. This is shown in Fig. A.4. However, differences at this scale can be neglected.

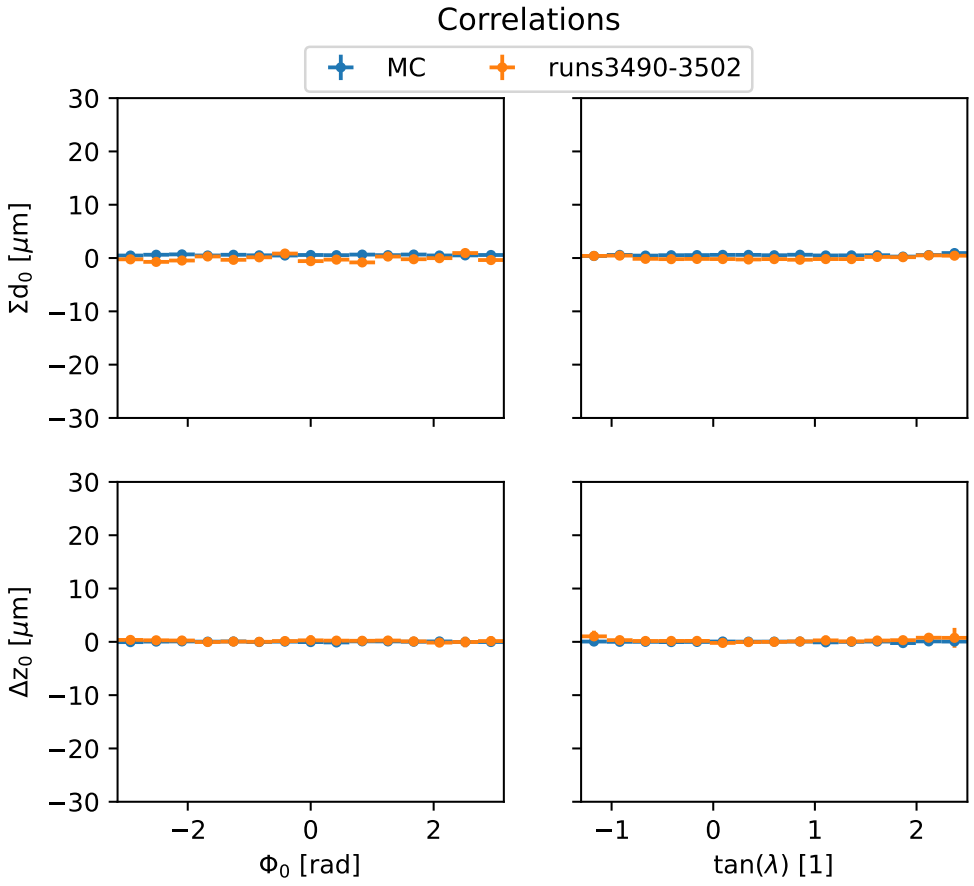


Figure 4.14: Correlations of the helix parameters of muons from collisions.

The histogram correspoinding to Fig. 4.14 can be found in Fig. A.5.

### 4.2.3 Resolutions

The maps of the resolutions of the parameters $d_0$ and $z_0$ for 'runs3490-3502' can be seen in Fig. A.6 and Fig. A.7. The stripes of lower resolution on them are exactly in the same spots as we have seen in the MC. This further gives credibility to our hypothesis that they are caused by the structure of the VXD.

In Fig. 4.15 all resolutions are slightly worse for 'runs3490-3502' than for MC. The difference in resolution is constant across all parameters. This is an expected result, as simulation represents the best possible outcome and real measurements are affected by various effects reducing the resolution such as misalignment.

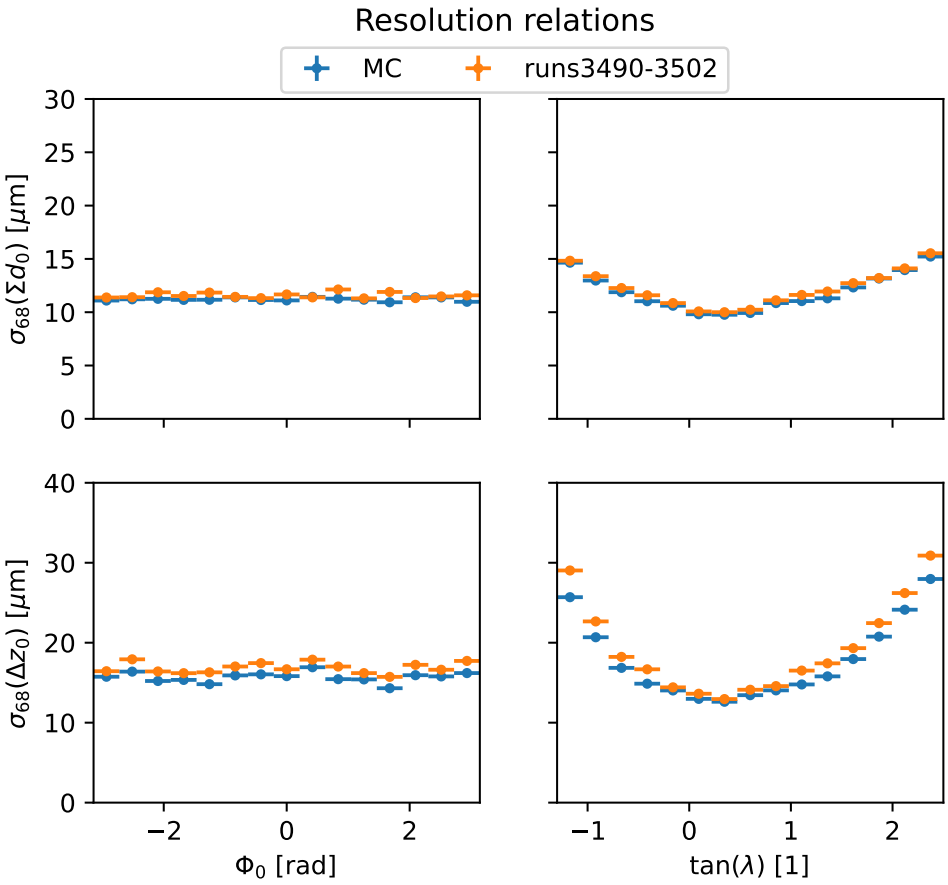


Figure 4.15: Resolutions of $d_0$ and $z_0$ with respect to the helix parameters.

Resolutions of $d_0$ and $z_0$ with respect to pseudomomentum can be seen in Fig. 4.16. Both 'runs3490-3502' and MC have been drawn with the same binning that was introduced in subsection 4.1.3 and fitted with the function 4.7.

For 'runs3490-3502' the results of the fit for $d_0$ are:

$$a = (9.82 \pm 0.13)\mu\text{m}$$

$$b = (16.10 \pm 0.84)\mu\text{m}\,\text{GeV}/c$$

And for $z_0$:

$$a = (13.38 \pm 0.20)\mu\text{m}$$

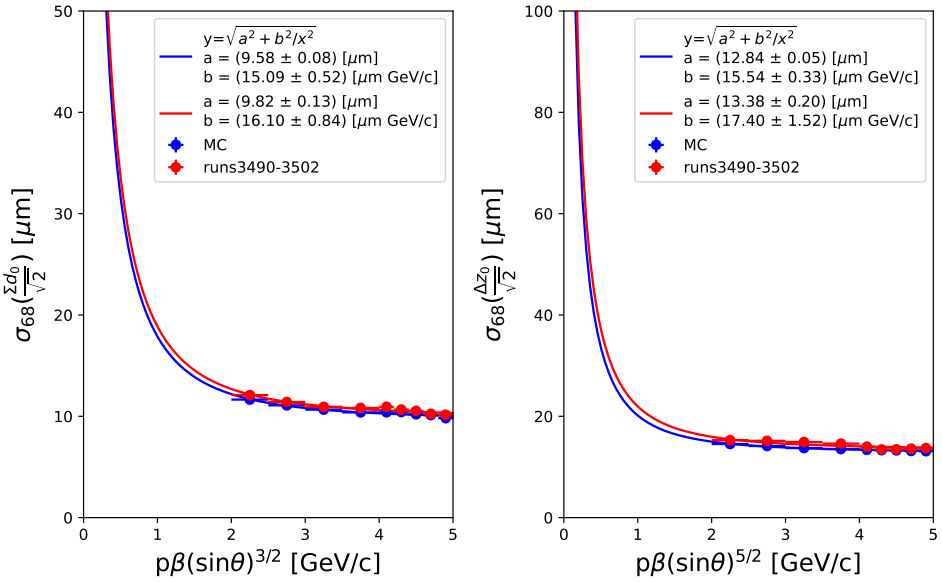


Figure 4.16: Resolutions of $d_0$ and $z_0$ with respect to pseudomomentum.

$$b = (17.40 \pm 1.52)\mu\text{m}\,\text{GeV}/c$$

The resolutions for 'runs3490-3502' are slightly worse just like in the previous plots. The differences in fit parameters $a$ and $b$ are all statistically significant except for the parameter $b$ for the resolution of $d_0$. But the difference is so small that it can be said that the detector is approaching its theoretical resolution limit.

## 4.3 Detector without the PXD

Near the end of the year 2024 the Pixel Detector has been turned off at Belle II for safety reasons due to sudden beam loss. Such an event could cause irreversible radiation damage to the PXD. This gives us an opportunity to examine how the resolution changes without it, as it is one of the main components responsible for the extreme tracking precision of the Belle II detector.

The data presented is from experiment 32 runs 100 to 110. This corresponds to 12.5.2024 to 13.5.2024. This dataset contains 160 429 events, it will be denoted as 'pxd-off'. The distributions of the parameters can be seen in Fig. A.8 to A.9, they follow the same distribution as was seen in section 4.2.1. The correlation are in Fig. A.11.

Now we can finally examine the resolutions and how they change with the missing PXD. The resolution of the $d_0$ helix parameter with respect to angles is shown in Fig. 4.17. The structure of the VXD is clearly visible here.

Resolution of the helix parameter $z_0$ with respect to the angles is shown in Fig. 4.18. Here we can see two large stripes of significantly worse resolution, especialy at the edges of the detector. This could correspond to two ladders of the SVD. However, there is no good explanation, from the structure of the detector, for why these two ladders specifically would exhibit such reduction in resolution. This issue is currently being investigated.

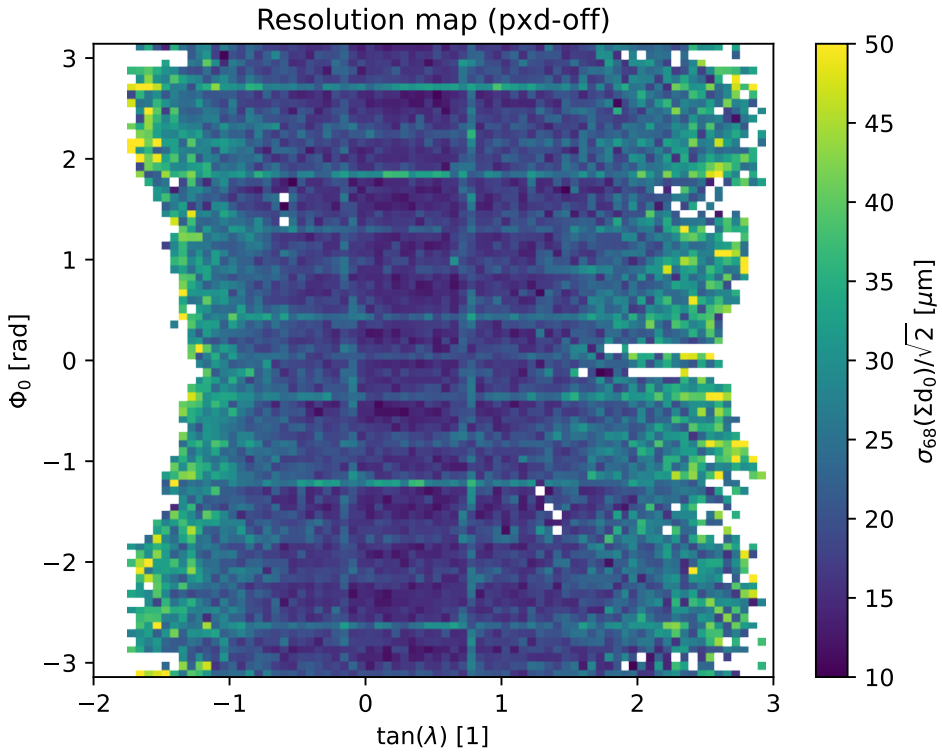


Figure 4.17: A map of the resolution of the helix parameter $d_0$ of muons from collisions while the PXD was off.

Resolutions of $d_0$ and $z_0$ with respect to pseudomomentum are shown in Fig. 4.19. The measured resolutions while the PXD was switched off were compared with the MC simulation. We can see that the resolution is more than 2× worse without the PXD. The resolution reduction in $z_0$ is even larger for low pseudomomenta.

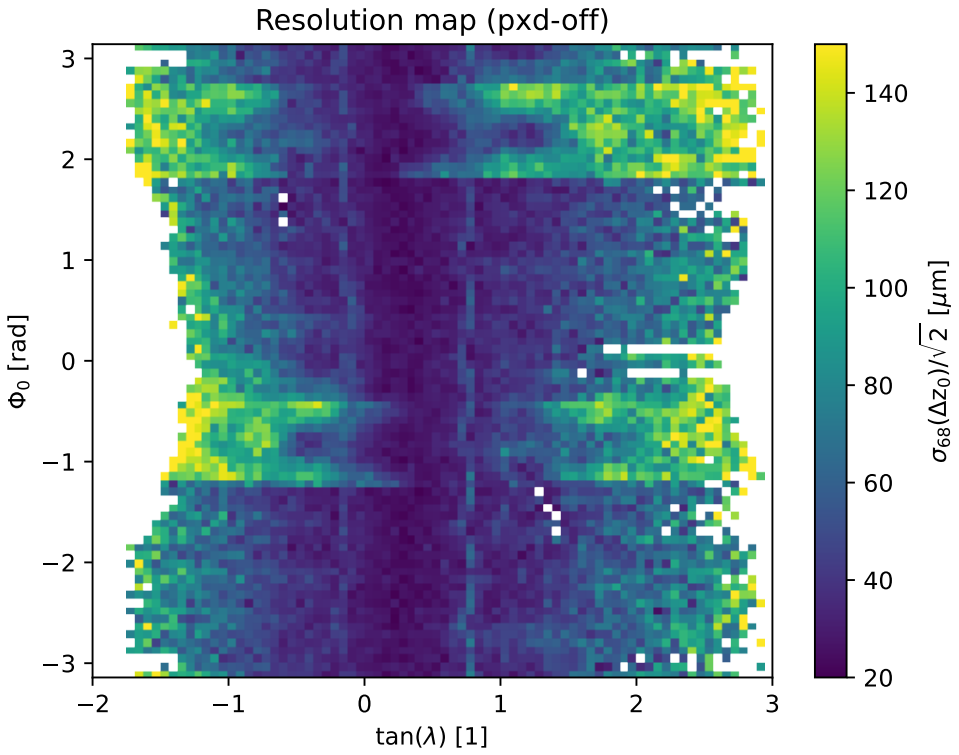


Figure 4.18: A map of the resolution of the helix parameter $z_0$ of muons from collisions while the PXD was off.

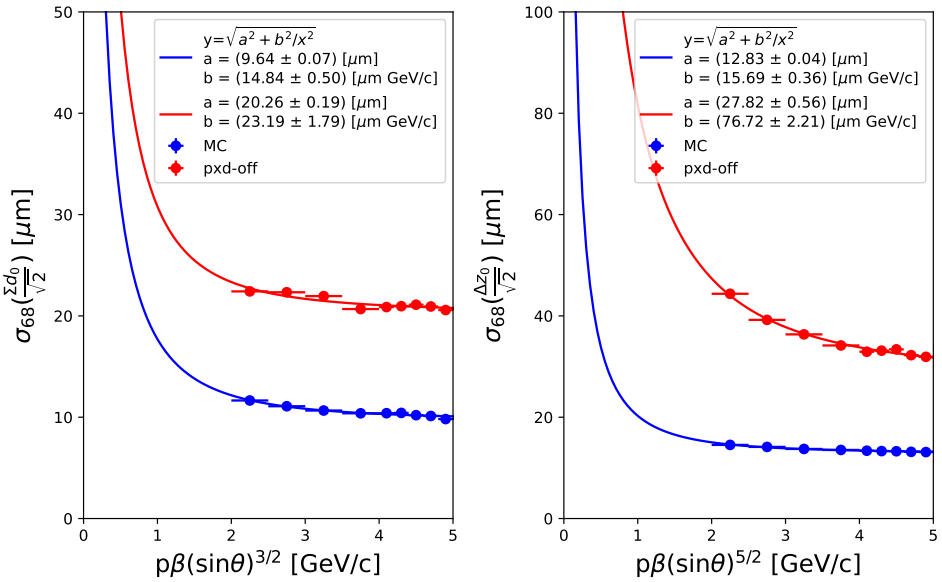


Figure 4.19: Resolutions of $d_0$ and $z_0$ with respect to pseudomomentum while the PXD was off.

For 'pxd-off' the results of the resolution fit for $d_0$ are:

$$a = (20.26 \pm 0.19)\mu\text{m}$$

$$b = (23.19 \pm 1.79)\mu\text{m}\,\text{GeV}/c$$

And for $z_0$:

$$a = (27.82 \pm 0.56)\mu\text{m}$$

$$b = (76.72 \pm 2.21)\mu\text{m}\,\text{GeV}/c$$

# Conclusion

In this thesis the studies of the Belle II detector performance were presented. The main focus was on the Vertex Detector and the alignment of the detector as they are crucial components for particle tracking.

In the review part of the thesis a brief introduction to particle physics and the motivation behind the Belle II experiment were given. They were then followed by a description of the SupereKEKB accelerator and the Belle II detector. The main parts of the detector were then described individually. At the end of this chapter the term 'alignment' and its importance were explained.

And in the next chapter we described our parametrization of the tracks and why muons were chosen for this study.

In the first experimental chapter we had the opportunity to examine the detector shortly after the completion of the Pixel Detector. The analysis was done using muons from cosmic radiation measured while the magnetic field inside the detector was disabled. Results with and without alignment were compared to understand how the alignment behaves after completion of the Pixel Detector. First the structure of the data was shown, in order to understand how cosmic muons interact with the detector. Then the correlations of the helix parameters describing the tracks of the muons were analyzed, to verify the quality of the alignment and ensure there are no non-physical biases introduced. Finally, the resolutions of the parameters were determined. After the completion of the Pixel Detector the performance of the detector and the alignment are optimal.

In the second experimental chapter the performance of the detector was evaluated using muons from $e^+e^- \to \mu^+\mu^-$ events. The first section was dedicated to examining the results of a Monte Carlo simulation of the collisions in order to introduce this type of data without any unexpected external influences. Similarly to the previous chapter the structure of the data was presented first. Then the correlations between the parameters were examined. Finally, the resolutions were determined. The whole area of the detector was examined for any sections with worse performance and the resolution with respect to pseudomomentum was determined. In the following section of the chapter, the measured data from collisions was compared with the previously shown results based on the Monte Carlo simulation. The resolutions of the measured data were slightly reduced, and the difference was statistically significant. However, the difference was small and the performance of the detector is approaching the theoretical maximum represented by the Monte Carlo simulation. The final section of this chapter examines the performance of the detector after the Pixel Detector has been switched off for safety reasons due to sudden beam loss. The resolution without the Pixel Detector is significantly reduced. A possible issue with two sections of the Silicon Vertex Detector has been identified and is currently being investigated.

# Bibliography


[1] Wikipedia - Standard Model [online]. [cit. 1.11.2024]. URL https://en.wikipedia.org/wiki/Standard_Model.

[2] J. H. Christenson, J. W. Cronin, V. L. Fitch, and R. Turlay. Evidence for the $2\pi$ decay of the $k_2^0$ meson. *Phys. Rev. Lett.*, 13:138–140, Jul 1964. doi: 10.1103/PhysRevLett.13.138. URL https://link.aps.org/doi/10.1103/PhysRevLett.13.138.

[3] V. Fanti, A. Lai, D. Marras, et al. A new measurement of direct CP violation in two pion decays of the neutral kaon. *Physics Letters B*, 465(1–4):335–348, October 1999. ISSN 0370-2693. doi: 10.1016/s0370-2693(99)01030-8. URL http://dx.doi.org/10.1016/S0370-2693(99)01030-8.

[4] Makoto Kobayashi and Toshihide Maskawa. CP Violation in the Renormalizable Theory of Weak Interaction. *Prog. Theor. Phys.*, 49:652–657, 1973. doi: 10.1143/PTP.49.652.

[5] E. Kou, P. Urquijo, W. Altmannshofer, et al. The Belle II Physics Book. *Progress of Theoretical and Experimental Physics*, 2019(12), dec 2019. doi: 10.1093/ptep/ptz106.

[6] Ivan Heredia de la Cruz. The Belle II experiment: fundamental physics at the flavor frontier. *Journal of Physics: Conference Series*, 761:012017, October 2016. ISSN 1742-6596. doi: 10.1088/1742-6596/761/1/012017. URL http://dx.doi.org/10.1088/1742-6596/761/1/012017.

[7] Kazunori Akai, Kazuro Furukawa, and Haruyo Koiso. SuperKEKB collider. *Nuclear Instruments and Methods in Physics Research Section A: Accelerators, Spectrometers, Detectors and Associated Equipment*, 907:188–199, November 2018. ISSN 0168-9002. doi: 10.1016/j.nima.2018.08.017. URL http://dx.doi.org/10.1016/j.nima.2018.08.017.

[8] Z. Dolezal, S. Uno, T. Abe, et al. Belle II Technical Design Report. November 2010.

[9] M Yonenaga, I Adachi, L Burmistrov, et al. Performance evaluation of the aerogel RICH counter for the Belle II spectrometer using early beam collision data. *Progress of Theoretical and Experimental Physics*, 2020(9), August 2020. ISSN 2050-3911. doi: 10.1093/ptep/ptaa090. URL http://dx.doi.org/10.1093/ptep/ptaa090.

[10] Tadeáš Bilka. *Time-dependent CP violation $B^0 \to \eta_c K_S^0$ decays at the Belle experiment, Alignment of the Belle II detector*. PhD thesis, Charles U., 2022.

[11] Valerio Bertacchi, Tadeas Bilka, Nils Braun, et al. Track finding at Belle II. *Computer Physics Communications*, 259:107610, February 2021. ISSN 0010-4655. doi: 10.1016/j.cpc.2020.107610. URL http://dx.doi.org/10.1016/j.cpc.2020.107610.

[12] Tadeáš Wilczek. Study of the Belle II vertex detector resolution. Bachelor's Thesis, Charles U., 2022.

# List of Abbreviations

**ARICH** Aerogel Ring-Imaging Cherenkov Detector

**basf2** Belle II Analysis Software Framework

**CDC** Central Drift Chamber

**CERN** European Organization for Nuclear Research

**CKM** Cabibbo-Kobayashi-Maskawa

**CMS** center-of-mass

**CP** Charge-Parity

**DEPFET** Depleted Field Effect Transistor

**ECL** Electromagnetic Calorimeter

**IP** interaction point

**KEK** The High Energy Accelerator Research Organization

**KLM** $K_L^0$ and $\mu$ Detector

**LHC** Large Hadron Collider

**LHCb** Large Hadron Collider beauty

**MC** Monte Carlo simulation

**mDST** mini data-summary table

**NP** New Physics

**PID** Particle identification

**POCA** point of closest approach

**PXD** Pixel Detector

**SM** Standard Model

**SVD** Silicon Vertex Detector

**TOP** Time of Propagation Counter

**VXD** Vertex Detector

# A. Attachments

## A.1 Cosmic Muons

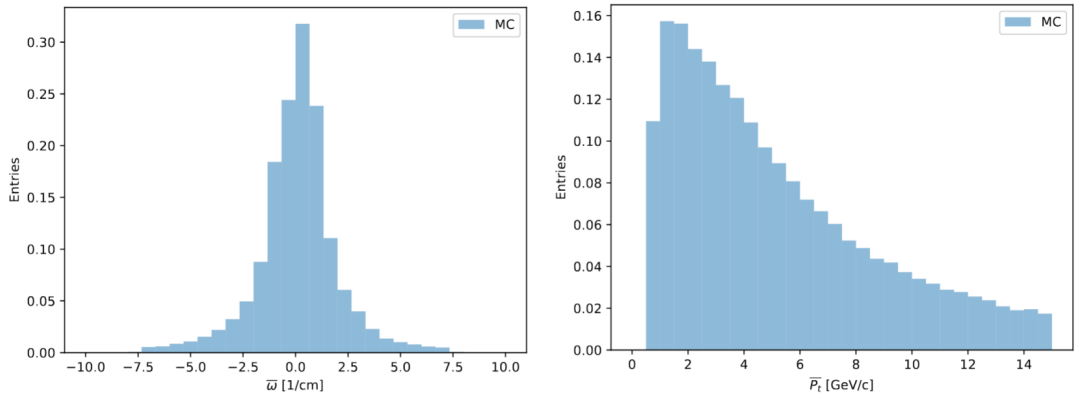


Figure A.1: Histograms of the track curvature $\omega$ (left) and transverse momenta $p_t$ (right) for cosmics. Taken from [12].

## A.2 Muons from the Monte Carlo Simulation

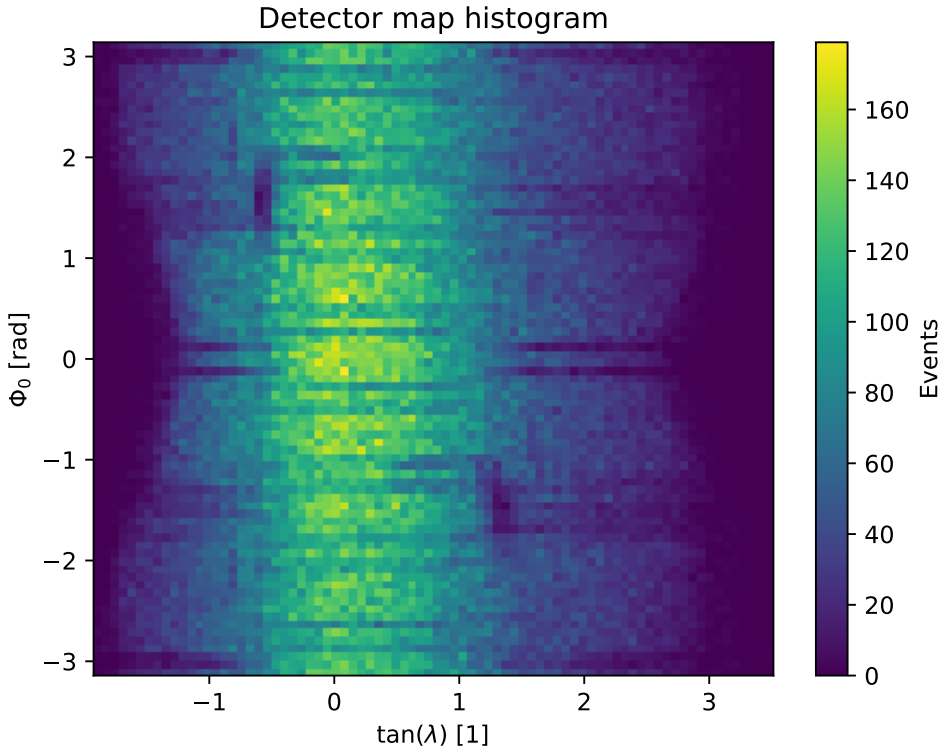


Figure A.2: Distribution of tracks for muons from colisions (runs3490-3502).

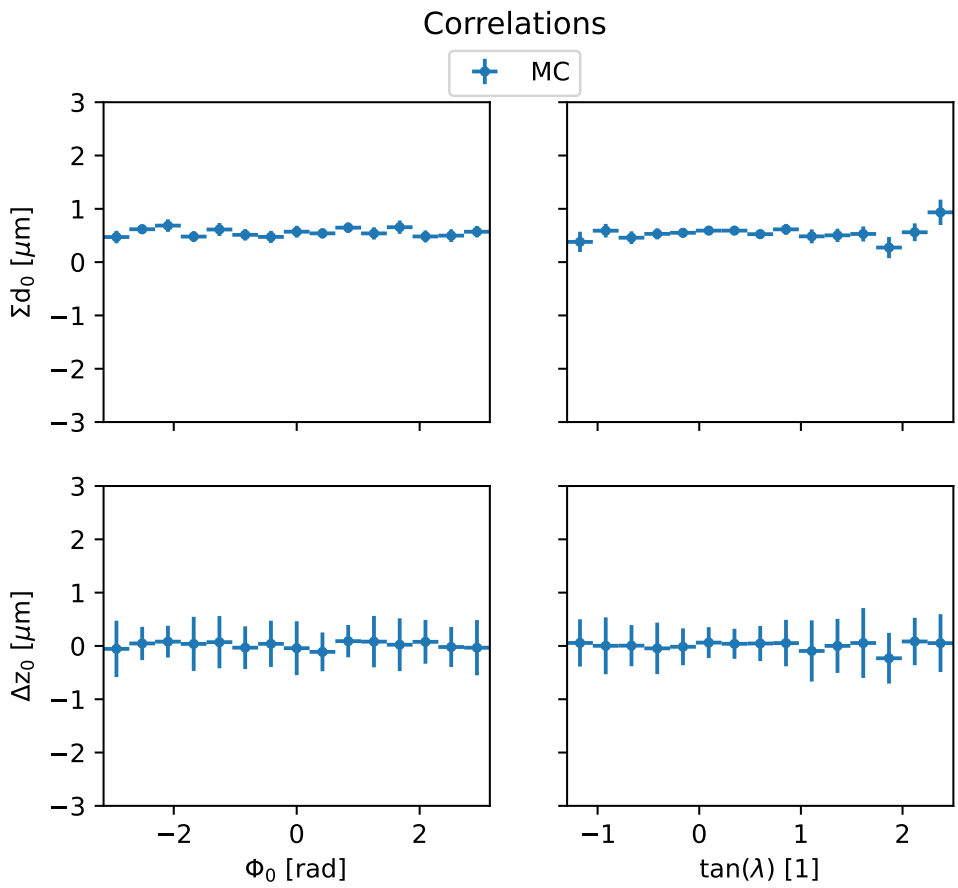


Figure A.3: Detail on correlations of the helix parameters for the MC.

## A.3 Muons from Collisions

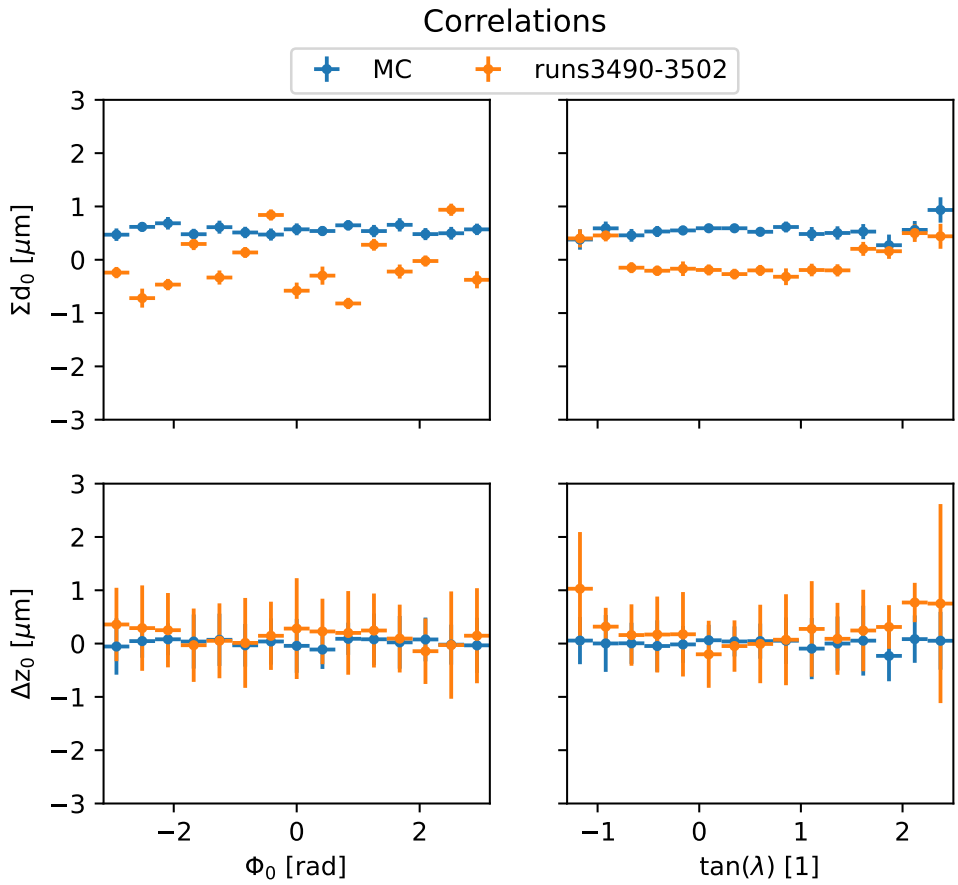


Figure A.4: Detail on correlations of the helix parameters for muons from collisions.

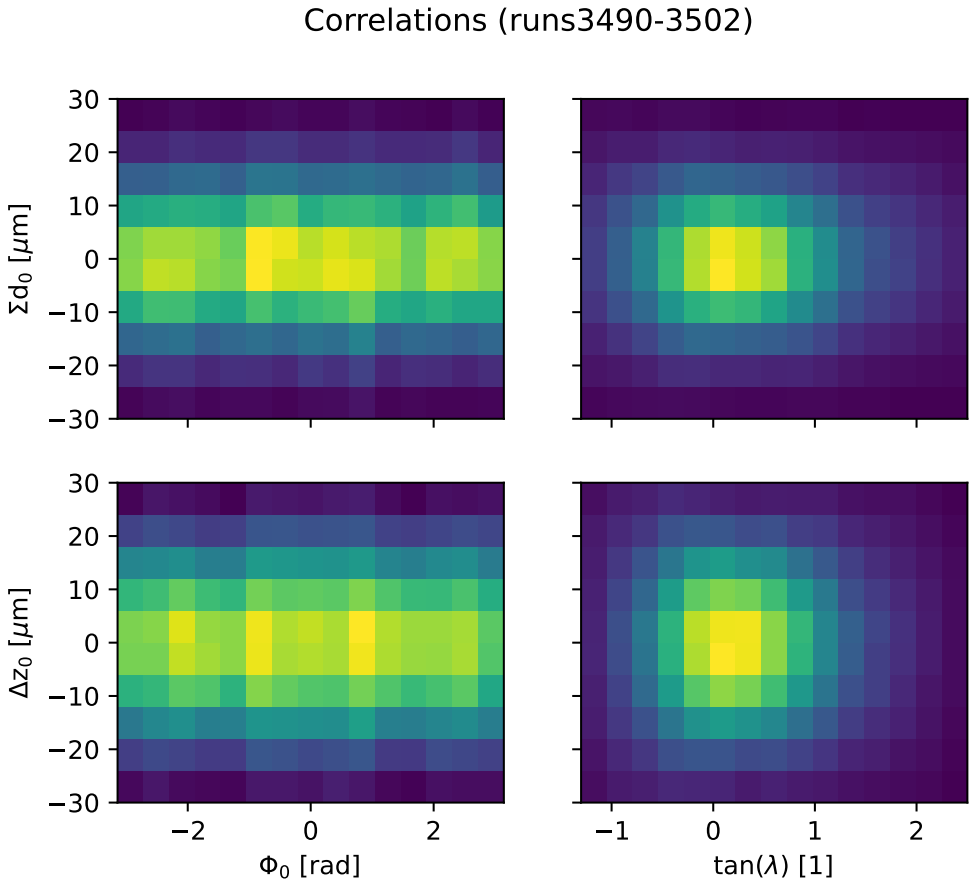


Figure A.5: Histogram of correlations of the helix parameters for muons from collisions.

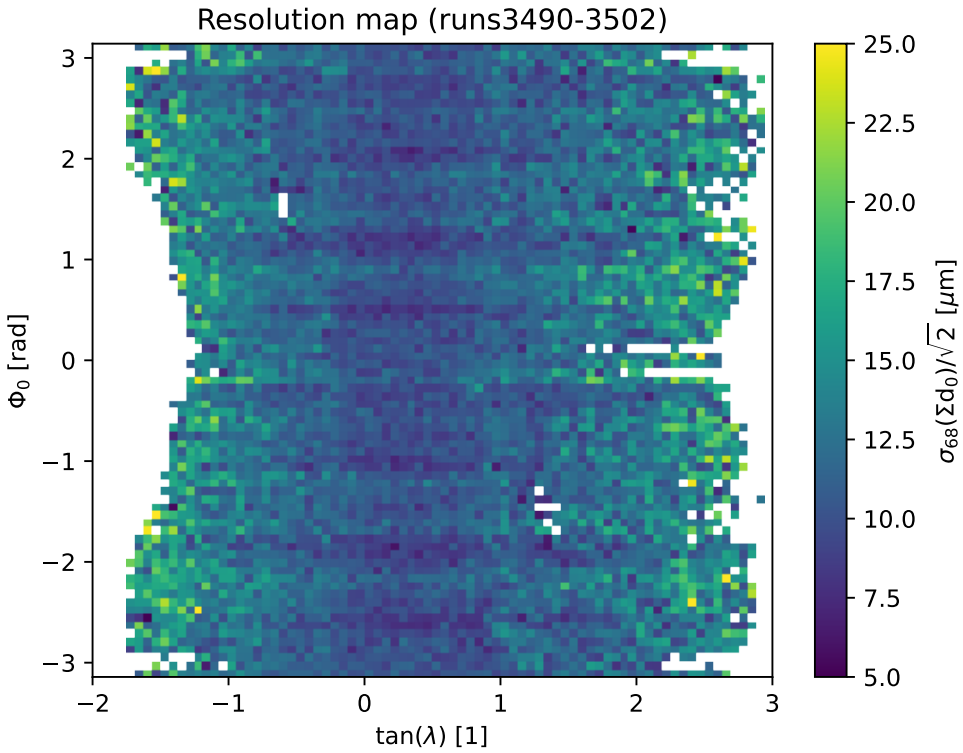


Figure A.6: A map of the resolution of the helix parameter $d_0$ of muons from collisions.

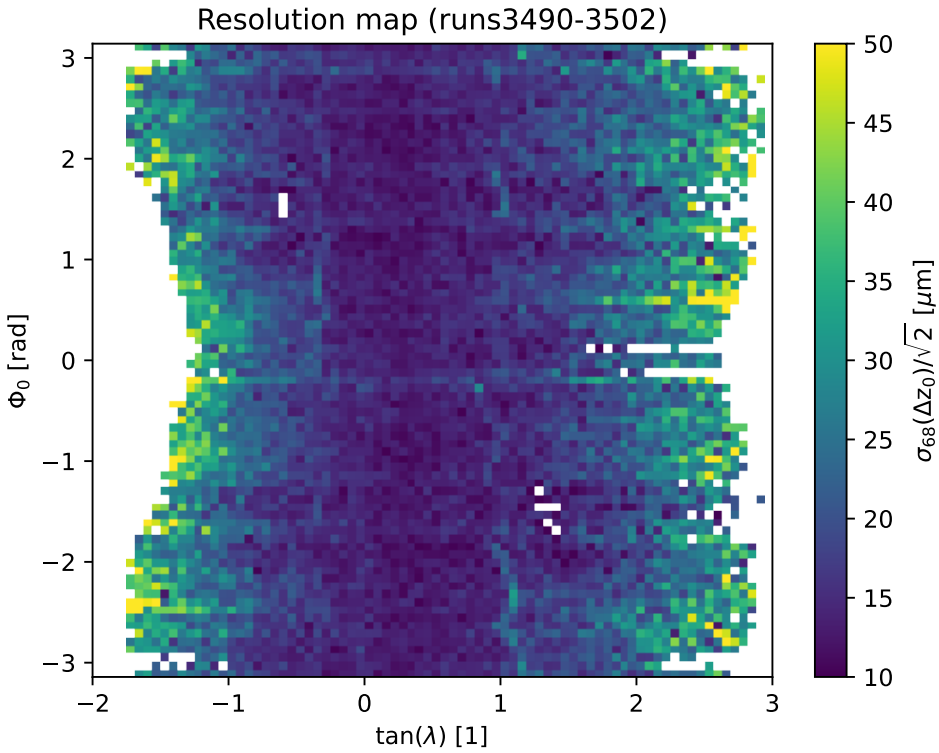


Figure A.7: A map of the resolution of the helix parameter $z_0$ of muons from collisions.

## A.4 Detector Without the PXD

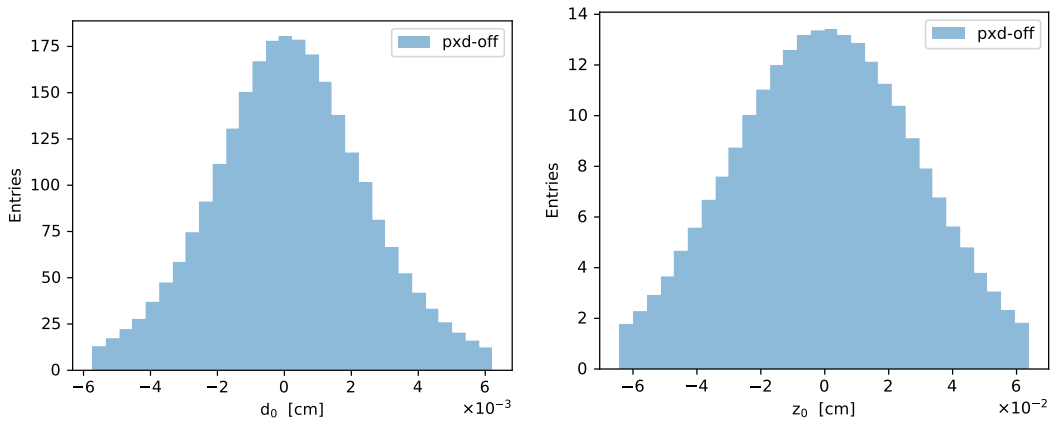


Figure A.8: Histograms of the parameters $d_0$ (left) and $z_0$ (right) for muons from collisions while PXD is off.

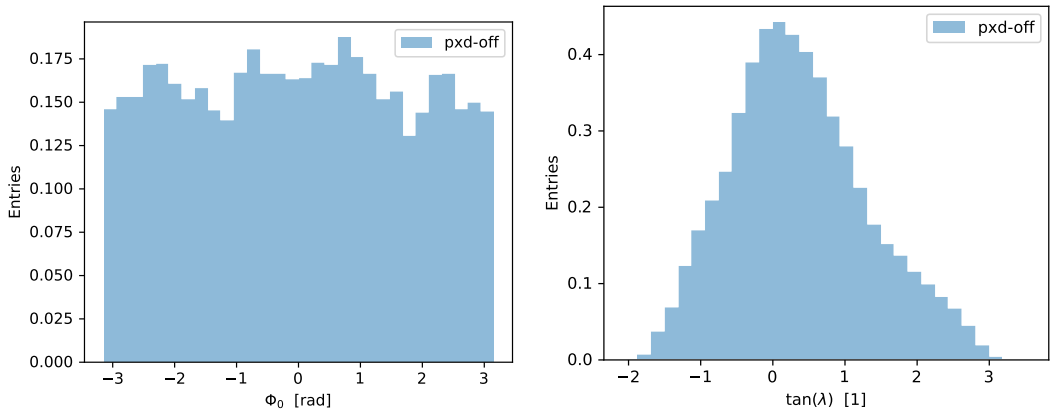


Figure A.9: Histograms of the parameters $\phi_0$ (left) and $\tan\lambda$ (right) for muons from collisions while PXD is off.

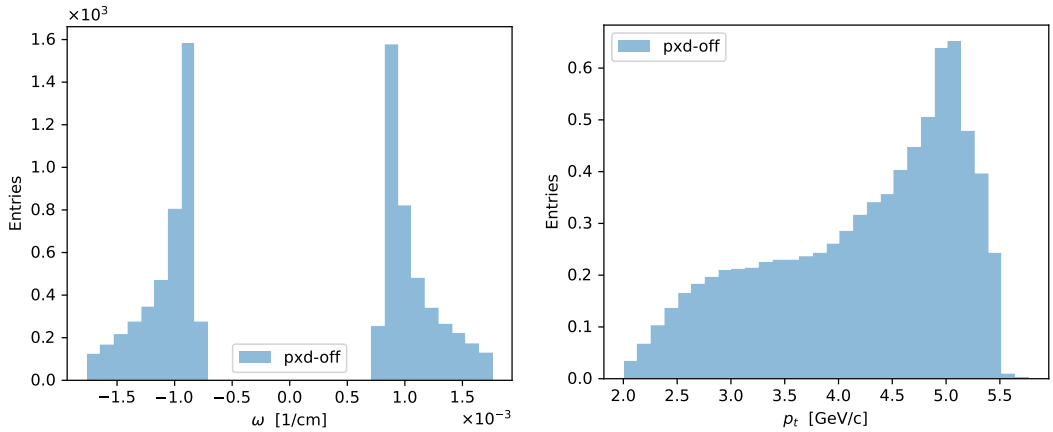


Figure A.10: Histograms of the parameters $\omega$ (left) and $p_t$ (right) for muons from collisions while PXD is off.

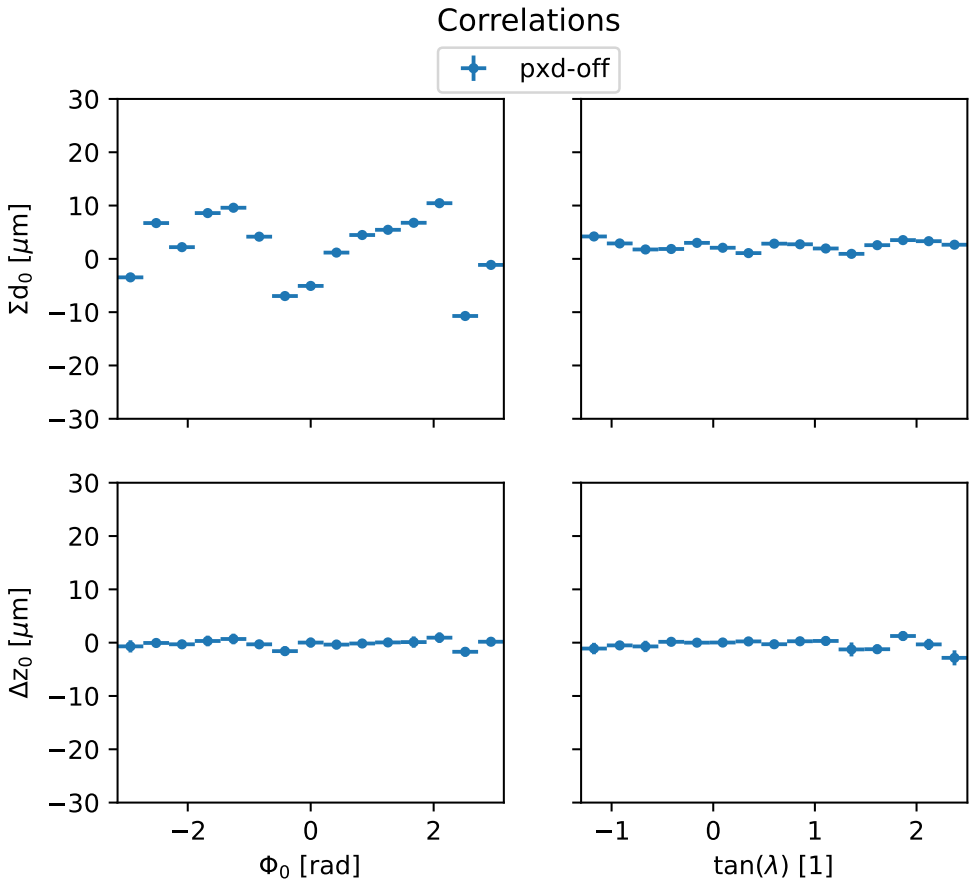


Figure A.11: Correlations of the helix parameters of muons from collisions while PXD is off.